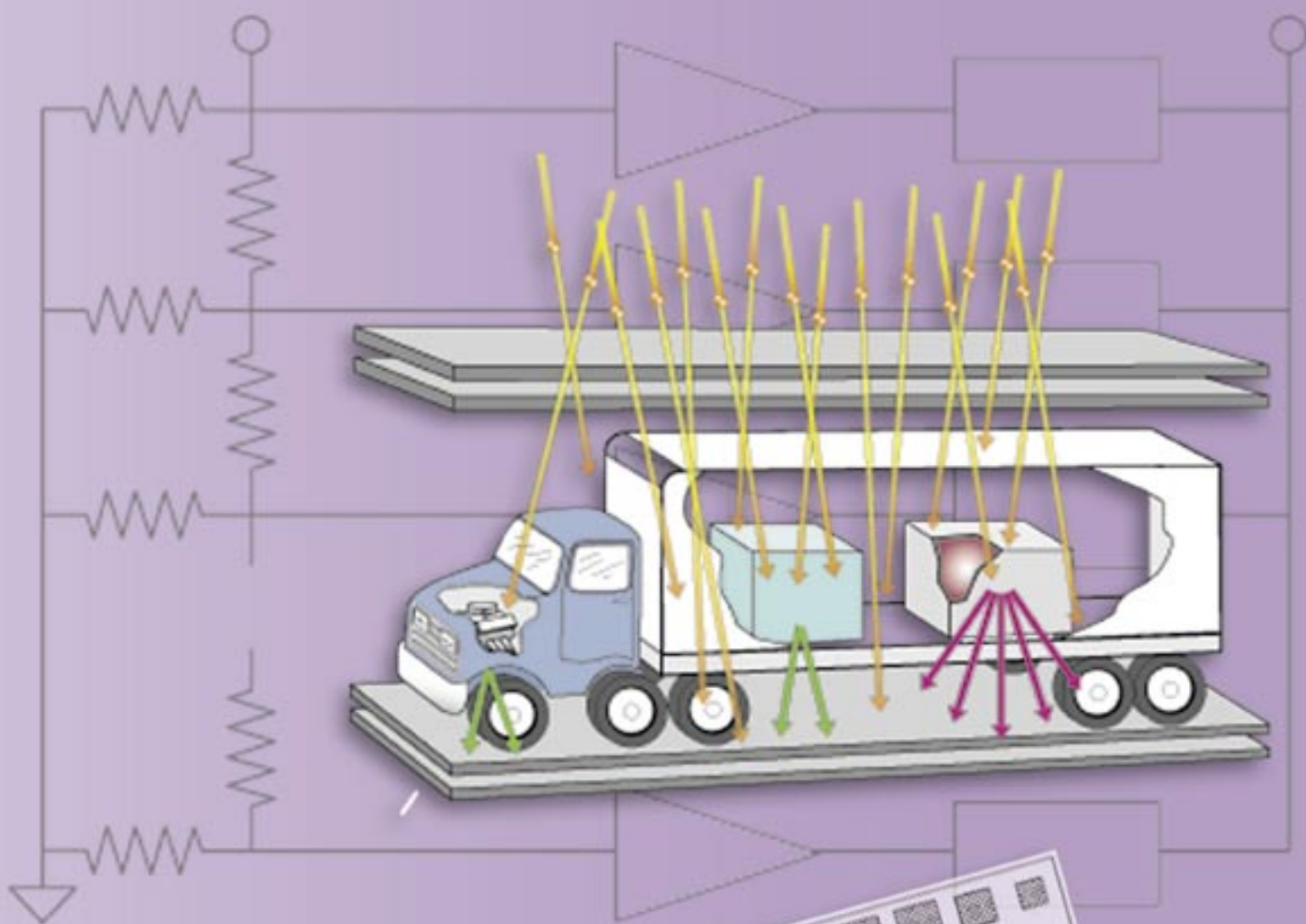


$$\alpha(t) = \frac{1}{V} \frac{dV}{dt} = \frac{d \ln(V)}{dt}$$

$$\sigma_{\theta} \approx \frac{15}{p} \sqrt{\frac{L}{L_{rad}}}$$

$$\frac{dV}{dt} = \alpha(t)V$$

# Instrumentation



$$V(t) = V_0 e^{\int_{t_0}^t \alpha(\tau) d\tau}$$

$$\frac{dn}{dt} = \alpha(t)n$$

# Instrumentation Contents

## Research Highlights

Electron Radiography	89
The Digital-Alpha Recording System	93
Applications of Antineutrino Detector Technology to Counterterrorism	97
A Large-Format Gated X-ray Framing Camera	101
Cosmic-Ray Muon Radiography for Homeland Defense	105

## Project Descriptions

Physics Measurements for DARHT-II Optimization and Risk Mitigation	109
Enhanced Test Readiness—Sub-Nanosecond Time Domain Electronics Enhanced Test Readiness Program	109
DynEx Confinement Vessel, Shipping Structure, and Cover-Installation Fixture	110
HPGe-Based Handheld Radioisotope Identification Instrument	110
W88 Pit Certification Red Team	111
Compton Gamma-Ray Imaging for High-Sensitivity Detection of Nuclear Materials	111
High-Definition Television	112
Laser-Based High-Resolution, High-Energy X-ray Imaging of High-Energy-Density Targets Using a Backlit Pinhole	112
The PHELIX “Transformer” for Proton Radiography Hydrodynamics	113
Low-Energy X-ray Radiography of Hydrotest Case Dynamics	113
Cygnus Radiographic X-ray Source	114
Advanced Plasma Diagnostic Concepts for National Magnetic Fusion Energy Research	114
40-mm, Gunpowder Breech Launcher for Proton Radiography Experiments	115
VISAR at pRad	115
Thermonuclear Burn Physics Using High-Energy Fusion Gamma Rays	116
KEYPATH: Using Atmospheric Turbulence to Generate and Exchange a Cryptographic Key	116
Interferometer Displacement Measurements of DynEx Vessel Oscillations	117
Advanced Detectors for Proton Radiography—Raising the Bar in Ultra-Fast Imaging	118
Reaction-History Reanalysis	119
Reaction-History Test Readiness	120
Support of Experiments at the Alternating Gradient Synchrotron	120
Generation of Energetic Ion Beams Using an Ultra-Short-Pulse, High-Intensity Laser	121



## Electron Radiography

An electron-radiography system, employing the charged-particle radiography technique, was built and commissioned in 2003 to demonstrate the capabilities of low-energy electrons to radiograph thin, static systems. The charged-particle radiography technique was developed with the 800-MeV protons at LANSCE<sup>1</sup> and 24-GeV protons at the Alternating Gradient Synchrotron (AGS) at BNL.<sup>2</sup> At these facilities, protons have been used to radiograph over 150 dynamic events and countless static objects.

At the front end of the electron radiography system, a “matched” electron beam is injected into the object to be radiographed. As the electrons pass through the object, they interact with the nuclei and electrons of the object, scattering the electrons away from their initial trajectory. After leaving the object, the electrons enter a magnetic lens quadrupole system that focuses the electrons back to an image, removing blur introduced by scattering within the object. A collimator, located at the center of the magnetic lens, is used to remove electrons that have been scattered to large angles within the object. The collimator removes fewer electrons passing through thin sections of the object than it does electrons passing through thick sections of the object. Therefore, the electron transmission at each position in the image provides a measure of the integrated density, or areal density, through the object. A schematic of the electron trajectories through the imaging system is shown in Figure 1. Electrons enter from the left, interact with a thin aluminum foil called a diffuser and are prepared for injection to the object as they pass through two matching quadrupoles. With no object in place, as shown in Figure 1(a), the electrons pass through the center of the collimator, and all electrons will arrive at the image location. In Figure 1(b), a scatterer has been placed at the object location. As the electrons pass through the object, they are scattered away from the injected trajectory. The collimator intercepts electrons that are scattered to large angles. Those electrons that pass through the collimator are refocused to an image at the image location. The measured electron transmission at each point at the image location can then be used to calculate an area density map of the object.

### Theory

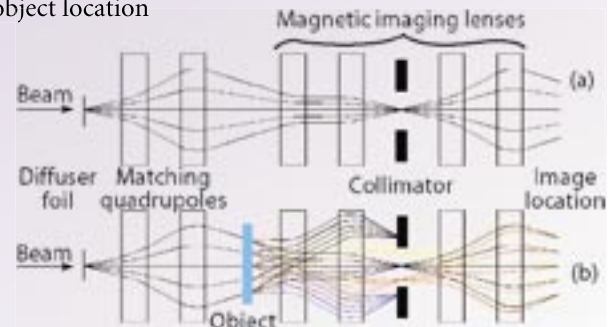
The magnetic imaging lens is setup in a symmetric Russian quadruplet configuration with alternating quadrupole gradients and is designed to provide a one-to-one map of the electron positions at the object location to positions at the image location. This mapping is described in Equation 1 in TRANSPORT notation:

$$x_i = R_{11}x_o + R_{12}x'_o, \quad (1)$$

where  $x_o$  and  $x'_o$  are position and angle at the object location,  $x_i$  is the electron position at the image location, and  $R$  is the first order TRANSPORT matrix. By choosing the

F.E. Merrill, C. Morris,  
A. Saunders (P-25),  
K.B. Morley (P-23)

Figure 1. Electron trajectories through the electron radiography imaging system. In Figure 1(a), electrons travel along their “ideal” trajectories because there is no scattering within an object. In Figure 1(b), electrons are scattered away from their ideal trajectory as they pass through the object. The electrons that are scattered to large angles are removed at the collimator location. Those electrons that pass through the collimator are reformed to an image at the image location.



## Instrumentation Research Highlights

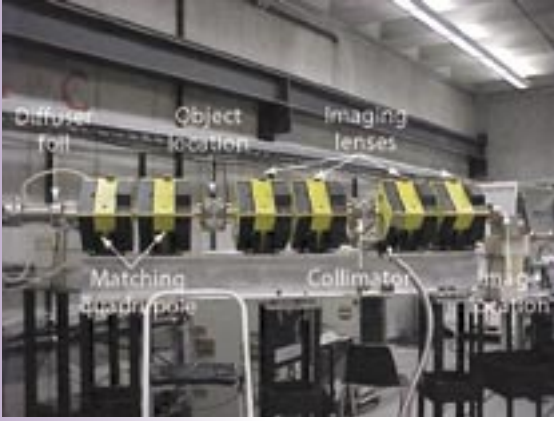


*Figure 2. The prototype electron-radiography system. The electrons from the accelerator enter from the left and are prepared for injection into the object by the diffuser foil and the first two matching quadrupoles. They then pass through the first half of the imaging lenses, a collimator, and the second half of the imaging lenses where they exit the vacuum jacket and form an image at the image location.*

quadrupole spacings and gradients so that  $R_{11} = -1$  and  $R_{12} = 0$ , we achieve the one-to-one mapping of electron position while also removing blur from scattering within the object.

As the electrons pass through the object, they also lose energy through interactions with electrons in the object materials. The resulting energy spread of electrons exiting the object makes second-order corrections important in the design of the radiography system. In addition to the first-order mapping (described above), Equation 2 shows the second-order mapping of electron position from the object location to image location:

$$x_i = -x_o + T_{116}x_o\delta + T_{126}x_o'\delta. \quad (2)$$

In Equation 2,  $T_{116} = \partial x_i / \partial x_o \partial \delta$  and  $T_{126} = \partial x_i / \partial x_o' \partial \delta$  are elements of the second-order TRANSPORT tensor, and  $\delta = \Delta p / p$  is the fractional momentum deviation away from the central momentum. When optimizing the resolution in the design of the electron-radiography system,  $\delta$  is determined by the thickness and composition of the object, and  $T_{116}$  and  $T_{126}$  are parameters of the lens system and cannot be adjusted without disturbing the first-order focus. Therefore, we must choose the position-angle correlation of the electrons entering the object, also called the matching condition, to be  $x_o' / x_o = -T_{116} / T_{126}$  to minimize the effect of second-order chromatic aberrations. With this matching condition, the remaining second-order contribution results from scattering in the object, which moves the electrons away from this ideal position-angle correlation. As the electrons pass through the object, they are scattered away from the matched trajectories by an angle,  $\theta$ . The resulting position mapping from object to image is shown in Equation 3. As shown by this equation,  $T_{126}$  becomes

the parameter that determines the ultimate position resolution of the electron-radiography system:

$$x_i = -x_o + T_{126}\theta\delta. \quad (3)$$

An additional requirement of the electron-radiography system is that the scattering angle within the object,  $\theta$ , is mapped to the radial position at the collimator location. This angle-to-position mapping will allow the precise removal of electrons that are scattered by the object to angles larger than the collimator cut angle,  $\theta_c$ . Equation 4 shows the mapping of position and angle at the object location to position at the collimator location,  $x_c$ . Here  $M$  is the TRANSPORT matrix from the object location to the center of the imaging lens at the collimator location:

$$x_c = M_{11}x_o + M_{12}x_o'. \quad (4)$$

If we prepare the position angle correlation at the object location  $x_o' / x_o = -M_{11} / M_{12}$ , Equation 4 becomes  $x_c = M_{12}\theta$ , which is a simple mapping of scattering suffered in the object to position at the collimator location independent of position at the object location. Mottershead and Zumbro<sup>3</sup> have shown that this correlation requirement is equivalent to the correlation needed to cancel the second-order chromatic effects as discussed above. The fortunate coincidence that the same position-angle correlation of the beam both corrects the chromatic effects and maps scattering angle to position at the collimator location has become known as the “Mottershead miracle” and is a characteristic of the symmetric Russian quadruplet lens system.

Because the requirements of a charged-particle radiography system are simple and the Russian quadruplet configuration meets these requirements in an elegant and compact way, a radiography system can be quickly and efficiently designed and constructed. To demonstrate the capabilities of electron radiography, a prototype system was designed, constructed, and tested using off-the-shelf components.

### Prototype System

Because of the development of low-energy electron accelerators by the medical industry for cancer-treatment therapy, the technology required to generate high currents of 20-MeV electrons is commercially available. The IAC in Pocatello, Idaho, has salvaged two of these accelerators from medical facilities and operates them for scientific use. The prototype of the electron-radiography system was therefore designed to use 20-MeV electrons from a Varian Clinac S-band accelerator, which operates at

2.9 GHz and provides a 3.25-mA average current for a pulse length ranging from 200 ns to 2  $\mu$ s. In this configuration, the Varian Clinac S-band accelerator can deliver up to  $4 \times 10^{10}$  electrons per pulse through the electron-radiography system.

The magnetic lens for the prototype electron-radiography system was designed to use an existing set of quadrupole magnets that were salvaged by the IAC from Boeing's Free-Electron Laser program. The lens system consisted of six quadrupole magnets. The first two magnets in combination with a diffuser foil setup the injection match to the object location. The remaining four magnets form the imaging lens with a collimator at the center of the radiography system and the image location at the exit of the vacuum system after the last quadrupole. A picture of the radiography system installed at the IAC is shown in Figure 2.

## Results from the Prototype System

The first radiographs that were collected with the prototype system were of a 1/16-in.-thick piece of aluminum with "LANL" machined through the plate. Figure 3 shows the results from the first series of radiographs with the prototype system along with a measure of the resolution from this radiograph. The "step" transition along an edge in the radiograph was used to determine the Gaussian line spread function, which was best fit with a Gaussian distribution having a root-mean-square width of 350  $\mu$ m as expected from the analysis of chromatic blur for this lens system as discussed above.

Because of their small mass, low-energy electrons are easily scattered. To demonstrate this sensitivity, a gold-marker pen manufactured by the Pilot pen company was used to write "eRad" on a piece of paper. The resulting radiograph of this paper is shown in Figure 4. The ink from this pen is 17% copper and the handwriting resulted in a layer of copper on the paper less than 0.001 in. thick. The ink was clearly imaged with  $\sim 20\%$  contrast. The radiograph also shows the  $\sim 5\%$  fluctuations caused by areal-density variations within the paper. Also shown in Figure 4 is a radiograph of the magnetic field from a flat dipole magnet similar to those commonly used to make refrigerator magnets. The electrons are scattered as they pass through the magnetic field of the dipole magnet, similar to multiple scattering within an object. These scattered electrons were then removed by the collimator and re-formed into an image mapping out the integrated magnetic-field strength of the dipole magnet.

An aluminum step wedge was also radiographed with a 10-mrad collimator (Figure 5) to demonstrate the capability of electron radiography to measure areal-density variations of thin systems. The three-step aluminum step wedge was constructed out of 0.0015-in.-thick aluminum foil, resulting in area densities of 10 mg/cm<sup>2</sup>, 20 mg/cm<sup>2</sup>, and 30 mg/cm<sup>2</sup>. A plot of the measured transmission across the step wedge (datapoints, blue) is also shown in Figure 5 along with a theoretical calculation of the expected transmission (solid line, red) based on the known areal density and collimator cut angle.

## Further Development

Encouraged by the success of the prototype electron-radiography system, a new effort, recently initiated, will improve spatial resolution and increase the penetration capabilities to extend this radiographic technique to thicker systems. The prototype electron-radiography system was designed to

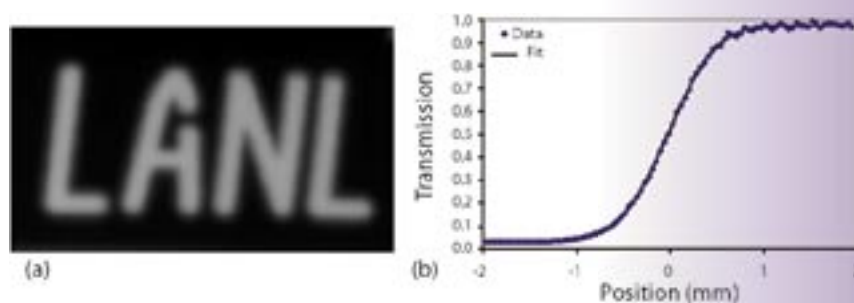


Figure 3. Results of the first radiographs collected with the prototype electron-radiography system. This is a radiograph of a 1/16-in.-thick piece of aluminum with "LANL" machined through the plate. The data points in Figure 3(b) show the measured transition in electron transmission across a sharp edge in the radiograph. The line is a fit to the data points assuming a Gaussian line spread function with a root-mean-square width of 350  $\mu$ m.

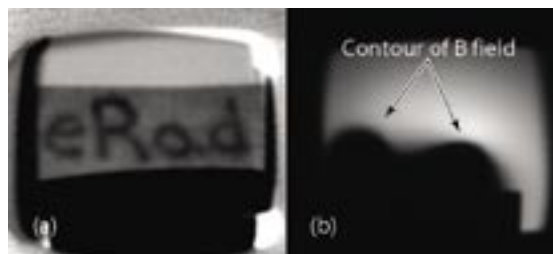


Figure 4. Figure 4(a) is a radiograph of "eRad" written on a piece of paper with a golden marker Pilot pen. This ink is 17% copper, and the writing resulted in a layer of copper less than 0.001 in. thick. The radiograph shows  $\sim 20\%$  contrast in the writing and 5% variations in the areal density of the paper itself. Figure 4(b) is a radiograph of a dipole magnet similar to those used to make refrigerator magnets. The radiograph shows contours of integrated field strength across the surface of the magnet.



## Instrumentation Research Highlights

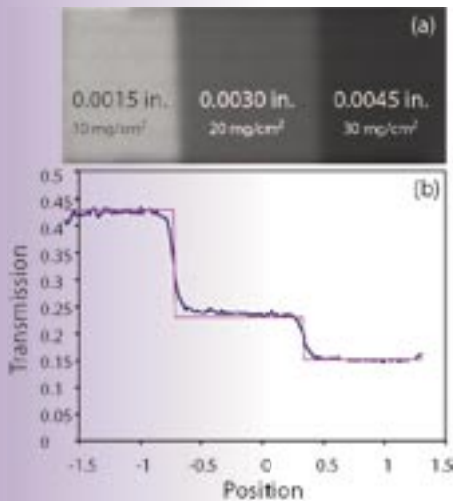


Figure 5. A 20-MeV electron radiograph of an aluminum step wedge with 0.002-, 0.004- and 0.006-in.-thick aluminum steps.

use existing quadrupole electromagnets available at the IAC. To significantly improve the resolution of the radiography system, the quadrupole gradient strength must be increased and the magnets shortened, as demonstrated by Mottershead *et al.*<sup>4</sup> with 800-MeV protons. Higher gradient and shorter quadrupoles are easily achieved through the use of permanent magnet quadrupoles. These magnets can be configured in a x5 magnifier geometry to improve the resolution of a 20-MeV electron-radiography system by a factor of five over the prototype system. The principles behind the magnifying electron-radiography system are identical to the identity lens system, but they introduce a magnification factor into the beam optics. Using these concepts, an electron-radiography system with commercially available permanent magnet quadrupoles has been designed and is being constructed.

Higher-energy electrons must be used to increase the penetration capabilities of electron radiography. The prototype system was designed for 20-MeV electrons because this energy is easily achieved with readily available electron sources. A program is under way to build a 40-MeV electron-radiography system that will also be constructed from readily available and existing accelerator structures and technology. In the future, a pulsed photocathode injector could be coupled to this 40-MeV accelerator to collect multiple radiographs of dynamic events within thin systems.

### Conclusion

A prototype electron-radiography system has been constructed and commissioned at the IAC. This prototype system successfully demonstrated the capabilities of low-energy electrons to image thin, static objects. The experimental measurements of spatial resolution and density reconstruction agree

well with models and theoretical predictions. With the proof-of-principle work complete, the concepts of charged-particle radiography are now being used to extend the capabilities of electron radiography to radiograph thicker systems with improved resolution.

### References

1. N.S.P King *et al.*, "An 800-MeV proton radiography facility for dynamic experiments," *Nuclear Instruments and Methods in Physics Research A* **424**, 84-91 (1999).
2. G.E. Hogan *et al.*, "Proton radiography," in *Proceedings of the 1999 Particle Accelerator Conference*, A. Luccio and W. MacKay, Eds. (IEEE, Piscataway, NJ, 1999), Vol. 1, pp. 579-584.
3. C.T. Mottershead and J.D. Zumbro, "Magnetic optics for proton radiography," in *Proceedings of the 1997 Particle Accelerator Conference*, M. Comyn, M.K. Craddock, M. Reiser, and J. Thomson, Eds. (IEEE, Piscataway, NJ, 1997), Vol. 2, pp. 1397-1400.
4. C.T. Mottershead, D. Barlow, B. Blind *et al.*, "Design and operation of a proton microscope for radiography at 800 MeV," in *Proceedings of the 2003 Particle Accelerator Conference* (to be published by IEEE).

### Acknowledgment

We would like to thank Tom Mottershead for his valuable insight and guidance in designing the prototype and magnifier lens systems. We would also like to thank Frank Harmon, the IAC director, for his support of these efforts and the support we received from the IAC staff: Brett King for his attention to detail while constructing the prototype system and Kevin Folkman for his untiring operation of the electron accelerator during our experimental campaigns. This work was funded by the LANL LDRD program.

For more information, contact Frank Merrill at 505-665-6416, fmerrill@lanl.gov.

## The Digital-Alpha Recording System

The digital-alpha waveform recorder, simply called “digital alpha,” is a specialized recording system (Figure 1) that has been customized to record optimally the exponentially increasing reaction history signal from a nuclear explosion. This technique uses a resistive voltage divider network to trigger a series of discriminators at pre-calibrated voltage levels. These discriminators provide the stop signal to time interval meters (TIMs)—which are precise digital clocks that share a common start signal in the digital alpha system. The output of the system is a set of voltage-time pairs that describe the input signal. Compared to other recording techniques, this system is easy to calibrate and use, and the data are recorded in a form that is easy to analyze. It has proved to be exceptionally stable when stored for over ten years and therefore may be easily maintained in a state of readiness in case of need.

Historically, the signal from a detector was recorded piecemeal by several Rossi oscilloscopes whose output is a Lissajous-like trace. One axis is driven by a stable time-reference oscillator; the other axis is driven by the signal from the alpha detector. The trace is recorded on film. Many Rossi oscilloscopes are needed to obtain a complete measurement, and a highly trained support staff is needed to operate and maintain them. The analysis of the data is time consuming and difficult—a great deal of effort is required to read the film and piece together the data. Nevertheless, this recording technique has been used on most nuclear tests and is the standard against which other systems must be judged. Much of the expertise in the use of Rossi oscilloscopes has been lost—or soon will be. Transient digitizers could, in principle, provide a modern replacement of these oscilloscopes. However, there are unresolved problems with digitizers because of their limited dynamic range and the lack of experience in using them to record reaction histories of nuclear events. Digital alpha is an automated, precisely calibrated system that is robust, is relatively easy to use, and produces data in a form that is easy to analyze and interpret.

The digital-alpha recording technique originated in the 1970s and was modernized in the late 1980s by the LANL high-speed electronics team and the electronics support group at EG&G (which is now Bechtel Nevada). Digital alpha was deployed on four nuclear tests—the results agreed to within about a percent with legacy systems. Although there is far less experience in operating this recording system than there is with oscilloscope-based techniques, digital alpha is intrinsically far simpler and will therefore more likely return data successfully with inexperienced operators than would a scope-based technique. Digital alpha should therefore be considered as a complement to, or replacement for, the usual reaction-history recording techniques. The system has been customized for reaction-history measurements by optimizing voltage-divider steps for the expected form of the signal. The system could be adapted to other fast-transient signals by customizing it in a similar manner—or by using it as is.

*J.D. Moses, S.K. Wilson  
(P-21)*

*Figure 1. Archival photo of the “digital alpha” system used in experiments at the NTS.*





### The Signal

The reaction-history signals are related to the rate of production of neutrons in a nuclear device, as follows:

$$\frac{dn}{dt} = \alpha(t)n, \quad (1)$$

where  $n(t)$  is the density of free neutrons in the device, and  $\alpha(t)$  is a multiplication rate, which depends on environmental variables such as the density of fissionable materials and therefore on time. We assume that our detector generates a current proportional to  $n(t)$  and that this current into a coaxial cable gives us the recorded voltage signal. It obeys the same equation as  $n(t)$ , whereby

$$\frac{dV}{dt} = \alpha(t)V \quad (2)$$

An operationally useful form of Equation 2 is

$$\alpha(t) = \frac{1}{V} \frac{dV}{dt} = \frac{d \ln(V)}{dt} \quad (3)$$

Alpha is the time derivative of the natural logarithm of the signal. The measurement of  $\alpha(t)$  is the reaction-history measurement. As long as  $\alpha$  is positive,  $\ln(V)$  (and therefore  $V$ ) increase monotonically with time. The voltage signal of interest is easily determined by integrating Equation 3, as follows:

$$V(t) = V_0 e^{\int_0^t \alpha(\tau) d\tau} \quad (4)$$

The signal from a given alpha detector typically has a dynamic range of about four orders of magnitude; it emerges from the noise at about 0.5 V and ends when the cable breaks down at around 4 to 5 kV. The bandwidth of a cable is typically about 50 MHz, but the usable bandwidth can be stretched to about 300 MHz by equalizing networks that extend the flat part of the cable-response curve at the expense of signal amplitude. It takes a number of detectors, each with its own recording system, to cover the entire range of the reaction.

### Digital-Alpha System Overview

As seen in Equation 3, a direct measurement of the logarithm of the voltage versus time is optimum for a measurement of alpha and has the additional advantage of extending the dynamic range of the system by logarithmic compression of the signal. It is hard to build logarithmic amplifiers of high precision, but it is straightforward to build voltage-divider networks with logarithmic increments and to calibrate these dividers precisely. This ladder network is customized for recording reaction histories.

The ladder in the network (Figure 2) is designed so that for each step the change in  $\ln(V)$  is constant:  $\ln(V_{n+1}) - \ln(V_n) = \ln(V_{n+1}/V_n) = r$ , or  $V_{n+1}/V_n = e^r$ . For the present network,  $r = 0.4$ . The voltage signal from each step of the ladder is fed into its own voltage discriminator, which generates a sharp timing pulse when its input threshold is reached. The TIMs have previously been given a common start signal and are stopped individually by the trigger pulse from their associated discriminator. Because the discriminator voltage threshold is calibrated, the stop times provide a time-versus-voltage measurement of the reaction-history curve. The TIMs can only be stopped once, so that the present system can only record the monotonically varying part of the signal (i.e., it works only as long as alpha does not change sign). The present TIMs have a time resolution of 50 ps, which is the time resolution of the system. The times are saved in nonvolatile memory so that the data can be read promptly—or later if that is more convenient. Both the timing circuits and the voltage divider network can be precisely calibrated using reference pulses; specialized calibration hardware has been built for this purpose. Alpha is simply expressed in terms of the data—it is the slope of the measured  $\ln(V)$ -versus-time curve. The error analysis is straightforward, and the result is a well-characterized and well-calibrated reaction-history measurement.

## Digital Alpha System Status

The present digital-alpha system was built during the last few years of underground nuclear testing and was under active development right up to the cessation of testing. It was then stored in pieces at Bechtel Nevada until about early 2002 when it was reassembled. Figure 3 compares a calibration of the ladder-discriminator network carried out in 1990 to a calibration of the same network carried out in 2003. The data are the ratios of voltages at adjacent positions in the ladder versus position in the ladder—both measured in powers of  $e$ . The ladder was built with 1% resistors. The large fluctuations around the design value reflect precision of the resistors. The repeatability of measurements of the ratio is about 0.2%, which is about the variation observed when the measurement is repeated after more than ten years. The system shows no apparent degradation in performance from storage over long periods.

## Conclusion

The digital-alpha system is well suited to be held in readiness for a resumption of underground nuclear testing over time scales of decades. It is stable, robust, and relatively easy to use. It provides data in a form that is easy to analyze and characterize; it can therefore be used and understood even after the present generation of experienced test personnel is unavailable. The system is also well suited for the measurement of other fast-transient signals, either by customizing the ladder network to match the expected form of those signals or by using the system as is to take advantage of its logarithmic-compression capability. Applications of this system to experiments other than nuclear testing should be explored further.

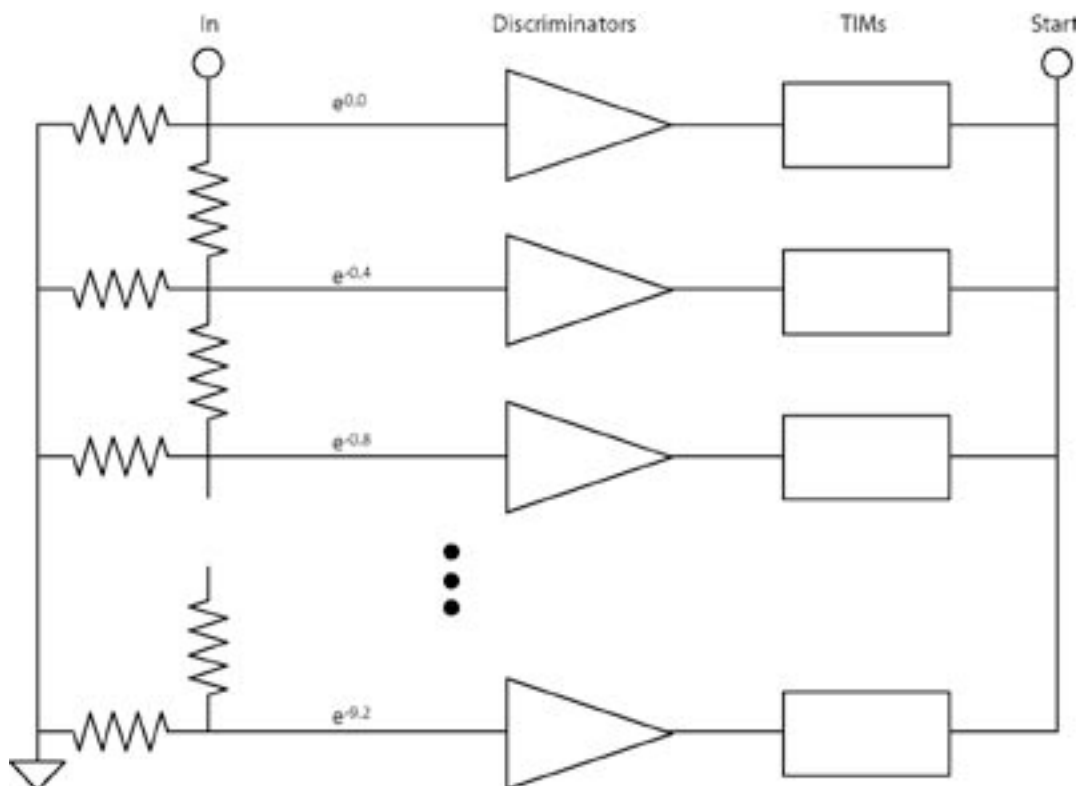


Figure 2. Schematic of the ladder-discriminator-TIM network. The TIMs are started with a common signal. They are individually stopped by the discriminators, which are triggered by the signals from the ladder. The attenuation factor at points in the network is indicated by numbers of the form  $e^{-x}$ .

## Instrumentation Research Highlights

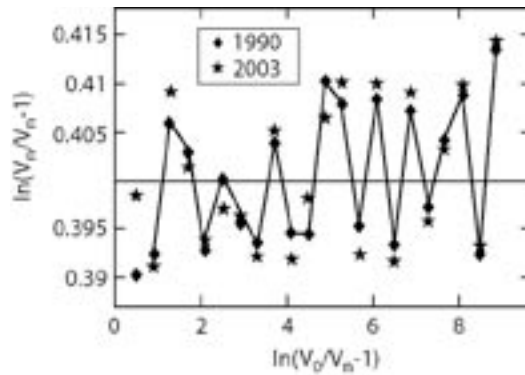


Figure 3. Calibration of the ladder-discriminator network in 1990 and 2003. The points represent the ratio of  $\ln(V)$  values at adjacent steps along the ladder network. The position along the network is given by the natural logarithm of the attenuation factor. The network was stable over the time that it was stored.

## Acknowledgment

The digital-alpha system was stored for twelve years at Bechtel Nevada; some of it was scattered over the NTS. Mike Carlisle (Bechtel Nevada) found all of the pieces of the system, including the system documentation and listings of the data-acquisition and control code. The system could not have been resurrected without his enthusiastic participation. Lyle Jensen and Kathy Breeding (Bechtel Nevada) made essential technical and archeological contributions. They represent much of the remaining expertise on the system hardware and software, respectively, and were invaluable participants in the early phases of this work. Eric Raby (P-21) showed remarkable skill and persistence in rewriting the ancient MSDOS and Windows data-acquisition and -control software to run under a modern operating system. P-21 consultant, Harvey Packard, was able to read the old computer backup tapes containing the design files for the calibration equipment so that these custom designs are not lost. This work was funded under the DOE Enhanced Test Readiness Program.

For more information, contact Samuel K. Wilson at 505-667-7823, [kwilson@lanl.gov](mailto:kwilson@lanl.gov).



## Applications of Antineutrino Detector Technology to Counterterrorism

The threat of highly organized and well-financed international terrorism requires the development of more sensitive, more versatile, and less expensive methods of detecting the presence of illicit radiological materials. The basic physics community has pioneered very large volume (kiloton) liquid-scintillator detector technology in recent years with the development of detectors for antineutrino physics.<sup>1,2</sup> Smaller-scale versions of “neutrino” detectors offer significant advantages over conventional detector technology for both stand-alone radiation monitoring and for use in active interrogation systems. The concept as applied to counterterrorism problems is called VLAN (Very Large Area Neutron Detector; the same acronym is used whether the application is for neutron or gamma-ray detection).<sup>3</sup>

*J.M. Moss, M.D. Cooper,  
G.T. Garvey, W.C. Louis,  
G.B. Mills, S.P. McKenney,  
R.E. Mischke, R.C. Schirato,  
R.G. Van de Water,  
N.L. Walbridge, D.H. White  
(P-25)*

### Advantages of Neutrino-Detector Technology

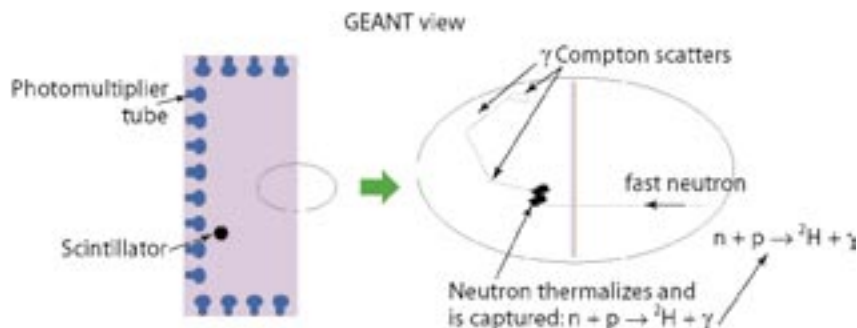
Current radiation monitors deployed at ports of entry and sensitive facilities such as military bases, reactors, and accelerators employ mature technology, typically plastic scintillators, <sup>3</sup>He proportional counters, or <sup>6</sup>Li-loaded glass for neutrons, and plastic scintillators and NaI(Tl) scintillators for gamma rays. Scaling this technology to large areas, required for increased detection sensitivity, is exceedingly expensive and cumbersome.

Some of VLAN’s advantages as a replacement for the older technology are listed below.

- It can be readily fabricated with large areas, 10 to 100 m<sup>2</sup> or more. This is an enormous advantage in detecting weak signals in passive applications. VLAN is inexpensive compared to competing detector technologies of comparable size and efficiency.
- Because it can be scaled to large sizes, VLAN is a logical component of future active-interrogation and neutron-radiography systems.
- VLAN is highly efficient for both fission neutrons (~ 30%) and MeV-range gamma rays (~ 70% full-energy peak). For detecting fission neutrons, VLAN employs a distinctive signal—a fast-neutron moderation pulse followed by the delayed capture of the 2.22-MeV gamma ray from the  $n + p \rightarrow {}^2\text{H} + \gamma$  reaction. The spatial distribution of this coincidence is also a strong discriminant against background events.
- Cosmic-ray muons are readily detected and identified as such by VLAN. Thus, variations in neutron backgrounds that follow variations in the cosmic-ray flux can be anticipated and valid-event selection can be correspondingly adjusted.
- VLAN is robust; simple to maintain; and may be easily calibrated, monitored, and operated remotely. Neutrino detectors using this technology have operated with virtually no component failure for five-plus years.

## Instrumentation Research Highlights

Figure 1. Schematic of VLAND. The enlargement at the right shows a simulated event using the CERN program, GEANT.<sup>4</sup> A neutron quickly moderates (thermalizes), followed by capture, which produces a 2.22-MeV gamma ray. The gamma-ray energy is absorbed by multiple Compton scattering.



### Neutrino-Detector Technology Applications

The basic unit thickness of VLAND is about a meter, set by the  $\sim 30$ -cm mean-free path of 2.22-MeV photons in a liquid scintillator. Given this condition, any number of configurations of VLAND are conceivable—depending on the specific application. Four possible applications are described below.

**As a fast-neutron portal monitor.** Figure 1 illustrates the concept for fast-neutron detection. The detector is a meter thick (horizontal dimension) with no photomultipliers on the sensitive (right) face. The detector's height and width may extend several meters. Fast neutrons enter and are moderated within 10 cm of the sensitive face, as is illustrated in the simulation detail at the right of Figure 1. The moderation signal (from recoiling protons) is detected for 25% to 75% of the fission neutron spectrum, depending on the number of photomultipliers and on the light-production efficiency of the scintillator.

Use of a several-square-meter fast-neutron detector would permit more stringent limits be placed on the amount of plutonium passing undetected through transportation portals than is possible with commonly used  $^3\text{He}$  proportional tubes. We could easily achieve gains in sensitivity by factors of 10 to 100. The fast-neutron signal is not subject to the large variation in background and innocent-radiation rates that plague gamma-ray-portal monitors.

**As a gamma-ray detector.** When used as a very large area gamma-ray detector, VLAND does not require the one-side-open geometry of Figure 1. Figure 2 shows a configuration that possesses directional sensitivity; such a detector could be mounted on a truck or a boat for large area search operations.

In order to be competitive with NaI(Tl) crystals, configurations that favor good energy resolution would be desirable. Because energy resolution is usually dominated by photon statistics, important factors in its optimization are large photomultiplier coverage and the use of an efficient scintillator. The KAMLAND collaboration<sup>2</sup> has already demonstrated an energy resolution of  $7.5\%/\sqrt{E}$ —about a factor of two inferior to that of  $4 \times 4 \times 16 \text{ in}^3$  NaI(Tl) crystals commonly employed in search applications. However, VLAND technology has a distinct advantage over NaI(Tl) because of its much more favorable peak-to-Compton-edge ratio. Within its fiducial volume, simulations show that VLAND would have a 70% photopeak efficiency. This would lead to spectral simplicity that facilitates separation of signal from background and from anthropogenic radiation sources.

**As an element of an active interrogation system.** In active interrogation, engineered sources of neutrons or high-energy photons are used to stimulate fission in SNM. Characteristic signatures of fission—delayed neutrons or gamma rays—are then recorded by a surrounding detection volume. Active interrogation is a known technology in the arena of nuclear safeguards; here long interrogation times are acceptable and comparatively small volumes need to be examined.

Currently no active interrogation system, even in the prototype stage, is applicable to the search for SNM in large transportation containers (truck trailers, shipping containers, etc.). Scaling the technology from the current  $\sim 1\text{-m}^3$  object size to that of transportation containers requires at least two major advances—more intense radiation sources and large area neutron detectors, such as VLAND (whether the interrogating source is photons or neutrons). Because delayed neutrons

## Applications of Antineutrino Detector Technology to Counterterrorism

are less energetic than those from fission, some optimization of the detection technology would be required. It may turn out, for example, that a modified VLAN using gadolinium-loaded scintillator would function better in this environment. Thermal-neutron capture on gadolinium yields readily identifiable  $\sim 8$ -MeV de-excitation gamma rays.

### *As an element of a fast-neutron radiography system.*

Conventional radiography using high-energy photons (nuclear gamma rays or bremsstrahlung from electron accelerators) is being increasingly deployed at critical transportation choke points to search for dense, heavy objects—objects that could be clandestine nuclear devices or components thereof. Muon radiography,<sup>5</sup> still in the research and development stage, promises sensitivity in this area as well.

Serious concerns remain about the ability of current radiographic methods (which were developed for conventional, not counternuclear, smuggling applications) to pick out small but significant quantities of SNM in transport containers in the presence of background clutter from legitimate cargo. A promising complement to current methods could be the radiographic application of fast neutrons.

Plutonium devices and kilogram-size quantities of plutonium are prolific sources of fast neutrons from spontaneous fission—readily detected by even unsophisticated portal monitors. However, when surrounded by a half meter of water or hydrogen-containing plastic, plutonium becomes nearly invisible to passive neutron detection. Highly enriched uranium (HEU, containing  $> 20\%$   $^{235}\text{U}$ ) presents a more complex challenge because it emits very few neutrons and primarily very low-energy gamma rays that are readily shielded by 1 cm of lead. However, the threat of active interrogation using neutrons and/or high-energy photons might well convince a would-be smuggler to protect his HEU with neutron shielding as well.

In contrast to photons, fast neutrons pass relatively freely through lead or iron, but are strongly attenuated in hydrogen-containing materials like water and polyethylene. This complementarity suggests the use of fast neutrons to search for the presence of neutron shielding in transportation vehicles. Figure 3 shows a simulated radiograph in which a shielded quantity of SNM in a  $2\text{-m} \times 2\text{-m}^2$  section of a shipping container is illuminated by a uniformly distributed source of 14-MeV neutrons.

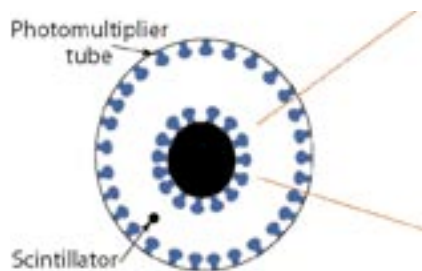


Figure 2. A possible configuration of a liquid scintillator tank for large area gamma-ray search application. The dashed lines indicate the approximate direction of sensitivity.

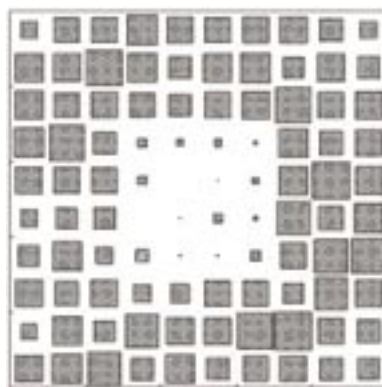


Figure 3. Simulated radiograph of a shipping container holding a shielded quantity of SNM surrounded by 50 cm of polyethylene. The white square in the center shows the outline of the neutron shielding. The contents of the container were simulated by a uniform mass of iron 10 cm thick (representing a container fully loaded to its 20-ton capacity).

Using fast neutrons to search for neutron shielding is fundamentally simpler than photon radiography for two reasons. First, moderation and containment of fission neutrons requires at least 50 cm of water equivalent, usually surrounded by a thin layer of thermal neutron absorber such as cadmium. Thus, the projected size of a shielded object is large—at least  $1\text{ m}^2$ —leading to a modest number of pixels required to characterize the area of a shipping container. Second, unlike photons, 14-MeV neutrons have a substantial probability of passing through thick objects, like fully loaded shipping containers, unscattered. Thus, rather than scanning the object with a well-collimated beam in order to minimize in-scattering from adjacent pixels, a large area beam may be used. In Figure 3,  $2.5 \times 10^5$  incident neutrons were used, which is a small fraction of the intensity available in one second from a commercial neutron generator.

A possible implementation of fast-neutron radiography could be as the second station following photon or muon radiography. A potentially threatening, but not completely convincing, dense object from the first radiograph would be examined at a second station with neutron radiography. The spatial overlap of the dense object in the photon radiograph with a region that contains substantial neutron shielding, likely to be a



## Instrumentation Research Highlights

rare circumstance in normal cargo, would signal the need for more detailed inspection of the container. Because of the simplicity of the neutron source and detector, fast-neutron radiography could be implemented for a fraction (perhaps 10%) of the cost of current photon-radiography stations.

### References

1. C. Athanassopoulos, L.B. Auerbach, D. Bauer *et al.*, “The liquid scintillator neutrino detector and LAMPF neutrino source,” *Nuclear Instruments and Methods A: Accelerators, Spectrometers, Detectors and Associated Equipment* **388**, 149–172 (1997).
2. K. Eguchi, S. Enomoto, K. Furuno *et al.*, “First results from KamLAND: Evidence for reactor antineutrino disappearance,” *Physical Review Letters* **90**, 021802(6) (2003).
3. J.M. Moss *et al.*, “Very large-area neutron detector (VLAND),” Los Alamos National Laboratory report LA-UR-03-1363.
4. R. Brun *et al.*, “GEANT3 (CERN 1987),” DD/EE/84-1 (revised).
5. K.N. Borozdin, G.E. Hogan, C. Morris *et al.*, “Radiographic imaging with cosmic ray muons,” *Nature* **422**, 277 (2003).

### Acknowledgment

DOE/NA-22 funding supported part of this work.

For further information, contact Joel Moss at 505-667-1029, [jmm@lanl.gov](mailto:jmm@lanl.gov).

## A Large-Format Gated X-ray Framing Camera

Gated x-ray imaging cameras have been a principal time-resolved x-ray instrument for the national Inertial Confinement Fusion/Radiation Physics (ICF/RP) program for over a decade.<sup>1</sup> Typically, these instruments use micrometer-size pinhole arrays to focus x-rays onto an image plane with the maximum usable image size limited by the height of the microchannel-plate (MCP) electrical microstrip. Most of the instruments currently in use have microstrips on 40-mm channel plates; with 4 or 2 separate strips to provide more time coverage, the image fields are only 6 mm tall with a few up to 15 mm tall.<sup>2</sup> A 6-mm-tall strip used with x12 magnification only allows a 0.5-mm-tall object to be imaged. This configuration causes the image to completely fill the strip and does not allow for any instrument misalignments. What most experimenters regularly do to compensate for the small image field is to focus onto that field with a lower-magnification pinhole configuration. This technique works fine until the experimenter requires higher spatial resolution or would simply like to image larger objects while maintaining resolution. We have designed, built, and fielded a gated x-ray framing camera that uses the equivalent of more than four normal-sized channel plates to provide a larger image plane—the Large Format Camera (LFC). While the LFC does have increased parallax compared to smaller-format systems, this camera (Figure 1) enables researchers to fully image objects from 1 mm to 6 mm tall (x12 to x2 magnification) with high spatial resolution, allows space on the imaging strip for slight misalignments, and provides greater temporal coverage.

Additionally, most gated instruments are constructed around standard 40-mm MCPs with 4 microstrips that can be gated independently. When acquired in a “heel-to-toe” configuration, this type of instrument gives researchers

*J.A. Oertel, T. Archuleta,  
M. Bakeman, P. Sanchez,  
G. Sandoval, L. Schrank,  
P. Walsh (P-24), N. Pederson  
(VI Control Systems)*

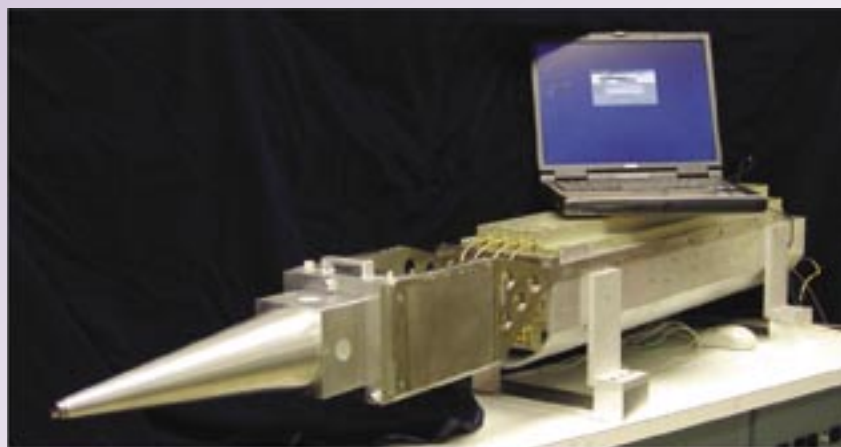


Figure 1. A photograph of LANL large-format x-ray imaging camera with its laptop-computer control system.

## Instrumentation Research Highlights

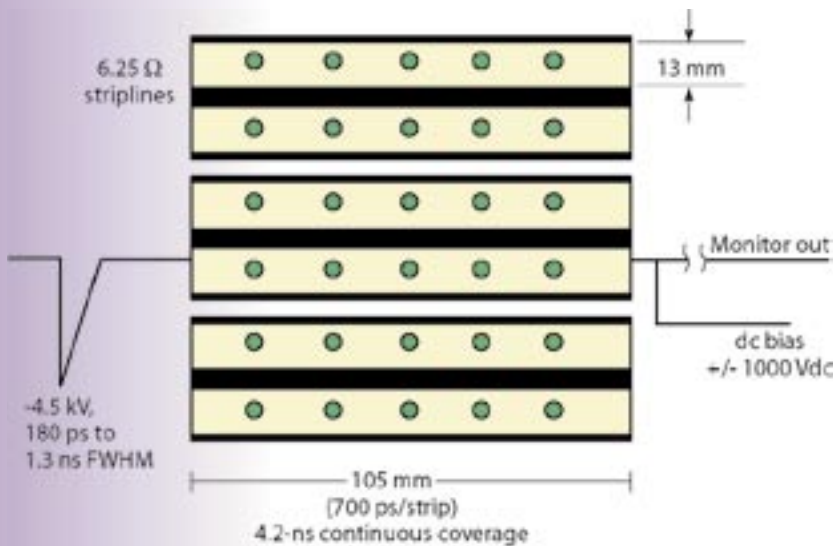


Figure 2. A front view of the gating process using three 105-mm  $\times$  35-mm MCPs.

a continuous data record up to 1 ns long. The temporal record is bounded both by the physical length of the microstrip and the propagation velocity of the electrical gating pulse. Researchers have worked around this instrumentation limitation by adding delay time between the individual microstrips and accepting the lost temporal information between the strip times.

For some experiments with a slower hydrodynamic evolution, the large interstrip timing technique is adequate and the missing data contains no useful information. But for fast-moving, long-duration ( $> 1$  ns) plasma events, longer continuous-record lengths can be critical.<sup>3</sup> The small-format design limitations in present instrumentation and the need to prototype technology for NIF instruments motivated the LANL ICF/RP program to fund the LFC.

The LFC design specifications are to provide

- (1) a 13-mm-tall microstrip on the MCP, which provides a large field of view with equal or improved spatial resolution;
- (2) six 105-mm-long microstrips, which enables a 4.2-ns continuous temporal record;
- (3) compatibility with any ten-inch instrument manipulator (TIM) or diagnostic insertion manipulator (DIM) (i.e., the TIM and DIM

are standard mechanisms used to insert instruments into ICF target chambers); and

- (4) a prototype for the future gated x-ray detector for NIF.

## Detailed Instrument Description and Specifications

As with conventional x-ray framing cameras, researchers can accomplish LFC imaging in many different ways. The standard pinhole imaging configuration for an LFC is also the simplest and least expensive.<sup>1,4</sup> Pinhole imaging uses small pinholes (typically 5 to 15  $\mu\text{m}$  in diameter) made of materials with a high atomic number, high-Z materials, such as tantalum or tungsten. Other methods of imaging include the use of a Fresnel zone plate, a grazing incident mirror, and crystal imaging.<sup>5,6,7</sup>

Gating of the image is accomplished by launching a short-duration, high-voltage electrical pulse across a microstrip transmission line on an MCP. A photoelectron signal produced at the front surface of the MCP photocathode is then exclusively amplified during the transit time of the voltage

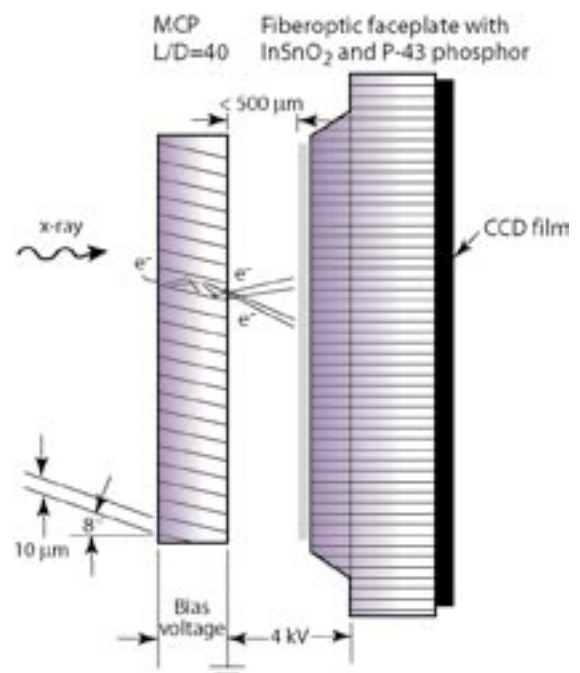


Figure 3. A side view of the MCP and phosphor screen.



pulse across a given point on the microstrip (Figures 2 and 3). By varying the width of the electrical gate pulse, the corresponding optical gate or shutter time can be varied proportionately.<sup>8</sup> This gives researchers increased flexibility in balancing appropriate shutter times and exposures with a plasma-physics experiment.

Amplification or gain of the signal in the MCP scales strongly with the applied pulsed voltage to a large power ( $G \sim V^9$ ).<sup>2</sup> The impedance,  $Z$ , of the microstrip on the MCP decreases with increasing height by the following equation:

$$\frac{w}{h} = \frac{2}{\pi} \left[ (d-1) - \ln(2d-1) \right] + \frac{\epsilon-1}{\pi\epsilon} \times \left[ \ln(d-1) + 0.293 - \frac{0.517}{\epsilon} \right]$$

where

$$d = \frac{59.95\pi^2}{Z\sqrt{\epsilon}}$$

and where  $w$  is the height of the strip,  $h$  is the dielectric thickness, and  $\epsilon$  is the effective dielectric constant.<sup>9</sup> The six 13-mm-tall (6.25 ohms), 105-mm-long microstrips require a custom impedance-matching circuit to drive the microstrip from a 50-ohm characteristic impedance. To date, the LFC incorporates a direct-impedance mismatch on the input side of the MCP. Although this is not the most voltage-efficient system, it was recognized as a high-fidelity alternative for propagation frequencies of interest. The output side of the MCP has been carefully designed to provide a path for MCP bias and to minimize reflections that could potentially double expose the image. Much of the impedance-matching network-development work tested (and eventually implemented) on this camera is directly applicable to NIF gated x-ray instruments.

The MCPs<sup>10</sup> and six tapers require a special housing or module in which to be enclosed (Figure 4). This module is designed to mechanically capture the MCPs to an exacting tolerance ( $\pm 0.001$  in.) with respect to each other and the fiberoptic faceplate. To accomplish this, a nonconductive, high-tensile-strength web supports both sides of the MCPs. This web is then retained in a stainless-steel structure that also serves as the ground plane and supports the vacuum electrical feedthroughs. The 112.5-mm<sup>2</sup> fiber-optic faceplate<sup>11</sup> is a composite of thousands of 6- $\mu$ m-diam fiber optics compressed together in

a coherent array. The fiber array is coated on one side with an indium tin oxide<sup>12,13</sup> conductive layer and then overcoated with a green P-43 phosphor to match the CCD sensitivity. As the amplified electrons stream out the back of the MCP array, they collide with the P-43 phosphor emitting visible photons to be collected with a CCD camera<sup>14</sup> or Kodak 2210 film.

The Kentech electronics designed to run this module are also very specialized.<sup>15</sup> The electronics unit provides computer control of the 6 MCP gate pulses and positive and negative direct current (dc) voltages to operate MCP and phosphor bias. Each of the 6 gate pulses can be biased independently, and a trigger-delay circuit enables timing control of each microstrip. Additionally, the high-voltage pulsers, used to gate the MCPs, can be pulse-width adjusted from 200 ps to 1300 ps. To determine the pulser voltage ( $V_{\text{pulser}}$ ) required to drive a 6.25-ohm strip ( $R_{\text{mcp}}$ ), the following equation is used:

$$V_{\text{mcp}} = V_{\text{pulser}} \Gamma_t = V_{\text{pulser}} \left[ 1 - \frac{R_{\text{pulser}} - R_{\text{mcp}}}{R_{\text{pulser}} + R_{\text{mcp}}} \right]$$

where  $\Gamma_t$  is the voltage transmission coefficient.<sup>9</sup>

The Kentech unit controls and monitors all electrical functions via an RS232 connection to a laptop-control computer. This Kentech unit will be very similar to the NIF gated x-ray detector system, and the software for that system is being prototyped on the LFC.

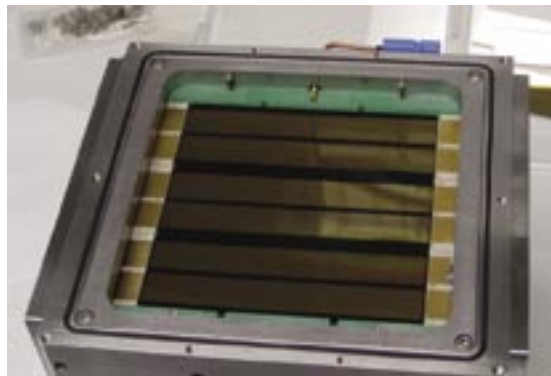


Figure 4. The LFC MCP module containing three 105-mm  $\times$  35-mm MCPs.

### Conclusion

The LFC is a new LANL x-ray imaging instrument designed to image large NIF-scale ICF/RP objects with a long, continuous temporal history, while maintaining equivalent spatial resolution relative to previous and current small-format instruments. The LFC camera has a 105-mm<sup>2</sup> active area with six 13-mm-tall striplines and a P-43 phosphor overcoat; it is then interfaced to a CCD camera. The electrical gate is variable from 200 ps to 1300 ps and is capable of continuous temporal records of 4.2 ns. This camera is also used to test and evaluate new technologies that will be applied to future NIF x-ray imagers.

### References

1. J.D. Kilkenny, "High speed proximity focused x-ray cameras," *Laser and Particle Beams* **9**(1), 49 (1991).
2. O.L. Landen, P.M. Bell, J.A. Oertel *et al.*, "Gain uniformity, linearity, saturation, and depletion in gated microchannel-plate x-ray framing cameras," in *Ultrahigh- and High-Speed Photography, Photonics, and Videography '93*, P.W. Roehrenbeck, Ed. (SPIE, Bellingham, Washington, 1993), Vol. 2002, p. 2.
3. C.W. Barnes, D.L. Tubbs, J.B. Beck *et al.*, "Experimental configuration of direct drive cylindrical implosions on the OMEGA laser," *Review of Scientific Instruments* **70**(1), 471 (January 1999).
4. A.J. Toepfer, L.P. Mix, and H.J. Trussell, "Pinhole imaging techniques for hard x-rays," (SPIE, Bellingham, Washington, 1977), Vol. 106, p. 47.
5. A.V. Baez, "Fresnel zone plate for optical formation using extreme ultraviolet and soft x radiation," *Journal of the Optical Society of America* **51**, 405 (1961).
6. F.J. Marshall, M.M. Allan, J.P. Knauer *et al.*, "A high resolution x-ray microscope for laser driven planar-foil experiments," *Physics of Plasmas* **5**(4), 1118 (1998).
7. F.J. Marshall and J.A. Oertel, "A framed monochromatic x-ray microscope for ICF," *Review of Scientific Instruments* **68**(1), 735 (1997).
8. J.P. Holder, D.R. Hargrove, T.S. Perry *et al.*, "Nanosecond gating of microstripline microchannel plate framing cameras: Characterization and simulation," in *Proceedings of the Ultrahigh- and High-Speed Photography, Photonics, and Videography '03 (Conference 5210)*, San Diego, California, August 7–8, 2003.
9. L.A. Trinogga, G. Kaizhou, and I.C. Hunter, *Practical Microstrip Design*, First edition (Ellis Horwood Publishers, Chichester, UK, 1991), p. 30 and p. 110.
10. BURLE Electro-Optics, Inc., Sturbridge Business Park, P.O. Box 1159, Sturbridge, MA, 01566.
11. INCOM, Inc., 294 Southbridge Road, Charlton, MA, 01057-5238.
12. Deposition Research Laboratory, Inc., 530 Little Hills Blvd., St. Charles, MO, 63301.
13. Lexel Imaging Systems, 1501 Newtown Pike, Lexington, KY, 40511.
14. Retriever Technology, 228 S. Saint Frances Dr., Building D, Suite 1, Santa Fe, NM, 87501.
15. Kentech Instruments, Ltd., Unit 9, Hall Farm Workshops, South Moreton, Didcot, Oxfordshire, OX119AG, UK.

### Acknowledgment

Our team would like to recognize the ICF/RP Program Office for supporting this work. We also wish to thank the Trident Laboratory laser crew and the Diagnostic Engineering and Operations Team, with special recognition of Cris Barnes and Scott Evans.

For more information, contact John Oertel at 505-665-3246, oertel@lanl.gov.

## Cosmic-Ray Muon Radiography for Homeland Defense

The threat of the detonation of a nuclear device in a major U.S. city has prompted research aimed at providing more robust border surveillance for contraband SNM. Existing radiographic methods are not only inefficient for the detection of shielded SNM but also involve radiation hazards. Members of P-25 in collaboration with NIS Division have invented a new method that could detect small quantities of shielded SNM in a short time using the natural process of multiple scattering of cosmic-ray muons as a radiographic probe (Figure 1). A chief advantage of this new method is that no artificial radiation dose is applied to the object being examined. We are currently examining how well the method works for complex homeland defense scenarios.

*L.J. Schultz, J.J. Gomez,  
G.E. Hogan, C. Morris,  
A. Saunders, R.C. Schirato  
(P-25), K.N. Borozdin  
(NIS-2), W.C. Priedhorsky  
(NIS-DO)*

### Cosmic-Ray Muons and Multiple Coulomb Scattering

The earth's atmosphere is continuously bombarded by primary cosmic rays, which are energetic stable particles, mostly protons (Figure 2). Interactions between these protons and atmospheric nuclei produce a shower of secondary cosmic rays, including many short-lived pions. These pions decay quickly to muons, which interact with matter primarily through the Coulomb force and have no nuclear interaction. The Coulomb force, which involves the attraction or repulsion of particles or objects because of their electric charge, removes energy from muons more slowly than nuclear interactions would. Therefore, muons can travel a great distance through the atmosphere. Some muons decay to electrons. There are other particles generated in the cascade, but the remnant of the secondary cosmic-ray cascade at the earth's surface is 90% comprised of muons.

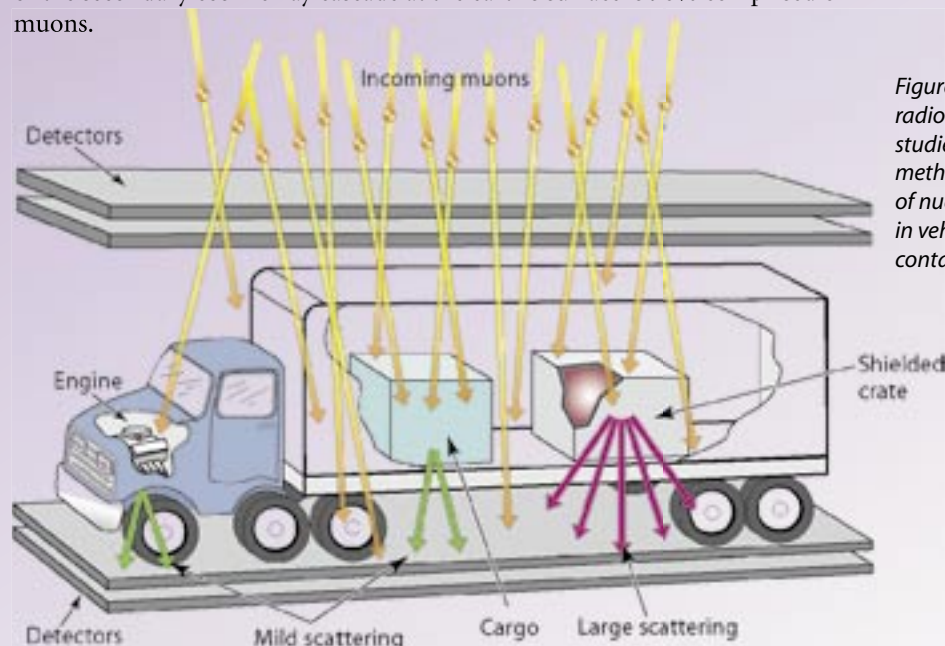
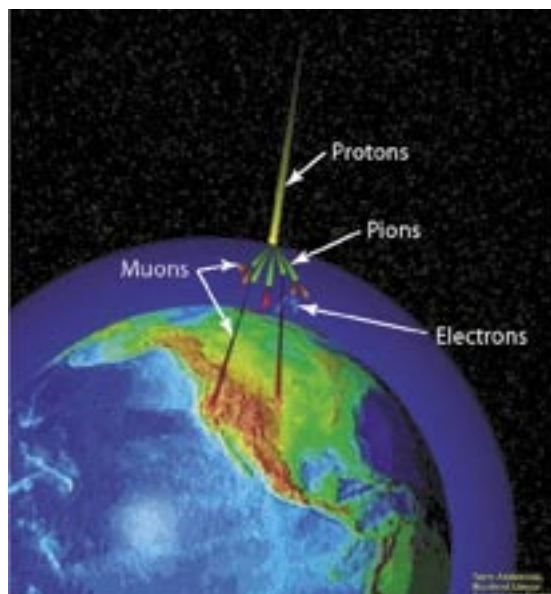


*Figure 1. Cosmic-ray muon radiography is being studied as a potential method for the detection of nuclear contraband in vehicles and shipping containers.*



## Instrumentation Research Highlights

Figure 2. Illustration of the atmospheric cosmic-ray particle cascade.



Consequently, the earth's surface is showered constantly by muons in the form of penetrating, weakly interacting charged radiation. Because about 10,000 muons per minute pass through each square meter of area (arriving from angles spanning the upper hemisphere), this shower of free particles was naturally considered as a radiographic probe. The mean momentum of muons at sea level is about 3–4 GeV/c, which allows them to penetrate through meters of rock. Because the momenta spectrum of the muons is continuous and the average range is long, differential attenuation can be used to radiograph large objects. In the late 1960s, Luis Alvarez placed muon counters below the Second Pyramid of Giza and used differential attenuation to search for hidden chambers within the structure.<sup>1</sup> Researchers continue to perform this type of radiography on large manmade and geographic structures.

### Calculating Uncertainty

One can calculate the uncertainty in this sort of radiography. The number of transmitted particles is  $N = N_0 \exp(-L/\lambda)$ , where  $\lambda$  is the mean-free path,  $N_0$  is the number of incident particles, and  $L$  is the depth of the material. The uncertainty in measuring  $L$  by counting transmitted particles is  $\Delta L = \lambda/\sqrt{N}$ . A 1,000-cm<sup>3</sup> volume of uranium would receive an incident flux of 100 muons in one minute. Because the mean-free path of cosmic-ray muons in uranium is on the order of 1 m, the thickness of a 10-cm cube of uranium could be determined to a precision of about its thickness.

Differential attenuation has proven useful for examining very large structures, but we make use of a different interaction between charged particles and matter to enable radiography of much smaller objects. A charged particle (such as a proton, electron, or muon) passing through material is deflected by many small-angle Coulomb scatterings off the nuclei of the atoms that make up the material. The particle will traverse the material in a stochastic path because of these multiple scatterings, and it will emerge at an angle scattered from the original track. The average scattering angle is distributed approximately Gaussian, and the mean-square scattering angle is strongly dependent on the material's Z number (i.e., atomic number, the elements in the periodic system are arranged in order of increasing number of protons in the nucleus) (Figure 3). There is a fairly clear distinction between the scattering from muon passage through common low-, medium-, and high-Z materials.

The width of the scattering distribution of muons is related to the scattering material as

$$\sigma_\theta \approx \frac{15}{p} \sqrt{\frac{L}{L_{rad}}},$$

where  $p$  is the particle momentum and  $L_{rad}$  is the radiation length. If the muon scattering angle in an object can be measured and if its momentum is known, then the material depth can be measured to a precision of  $\Delta L/L = 1/\sqrt{N}$ , where  $N$  (the number of transmitted muons) is very nearly equal to the number incident. Thus each transmitted muon provides information about the thickness of the object with a precision that is smaller than the thickness of the object. For the 10-cm<sup>3</sup> cube of uranium, for example, the uncertainty is 10% in one minute of exposure rather than the 100% that could be obtained with differential attenuation radiography. This analysis demonstrates the enormous advantage of multiple-scattering muon radiography for this application.

### Cosmic-Ray Muon Radiography—Experimental and Simulated Results

To make use of the information carried by scattered muons to probe an object, we tracked individual muons into and out of a target volume wherein objects to be radiographed are placed. (This work was carried out on Line B at LANSCE.) The scattering angle of each muon is measured, and we use tomographic methods to reconstruct

## Cosmic-Ray Muon Radiography for Homeland Defense

the structure and composition of the objects. To demonstrate proof of principle, we constructed a small experimental apparatus built with a set of four position-sensitive drift chambers. Two groups of detectors, each measuring particle position in two orthogonal coordinates, were placed above an object volume; two other groups of detectors were placed below. The position resolution of these detectors was measured to be about 400- $\mu\text{m}$  FWHM. Each radiograph of two small test objects shown in Figure 4 was made using the information carried by about 100,000 scattered muons. Several hours were required to produce the remarkable detail in these images using our small, relatively inefficient prototype. In a contraband detection scenario, only one or two minutes might be available for inspection. Fortunately, detection of shielded 5- to 10-cm-diam SNM objects requires many fewer muons. Moreover, the cosmic-ray muon momentum spread increases the uncertainty of the scattering signal in the experiment; however, we did not measure the muon momentum.

We have proposed a method of estimating muon momentum in an effort to further reduce exposure time. In this method, muon scattering is measured through plates of material of known depth and composition positioned below the object volume. To test this method, we developed a simulation code that generates cosmic-ray muons with the appropriate distribution of energies and angles, propagates them through a test volume, and generates the positions at which they would be detected in four detector planes. The muon spectrum, angular distribution, and rate were appropriate for sea level. A detector position resolution of 400- $\mu\text{m}$  FWHM was simulated, and the simulation was validated against the experimental results. Momentum measurement to about 50% precision was assumed.

We have examined numerous simulated scenarios wherein SNM contraband is placed within shipping containers that are hidden within various background cargos. Figure 5 presents the results of one of these simulations using a reconstruction method optimized for detecting high-Z material in medium-Z surroundings. A steel-walled cargo container containing 12 tons of distributed iron parts was simulated. One small lead-shielded container carrying a small amount of plutonium was placed within the cargo. The contraband is clearly visible in the one-minute simulated radiograph.

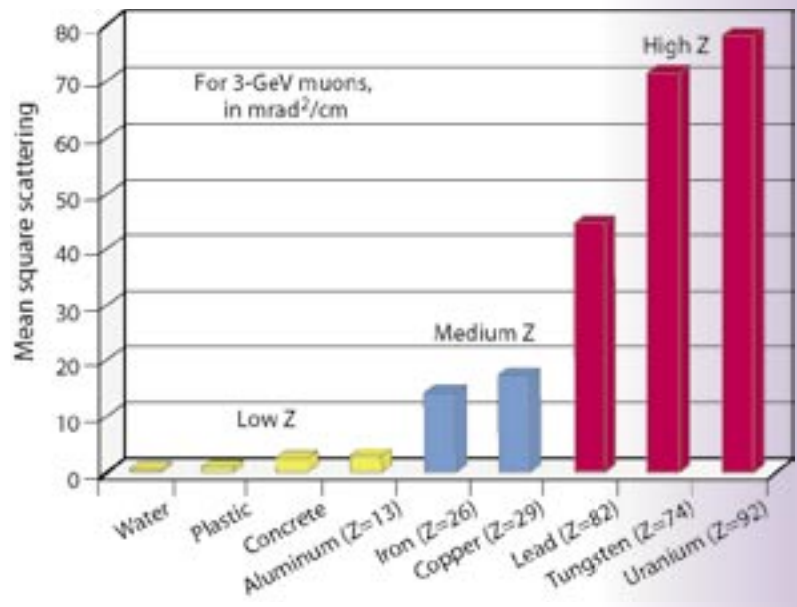
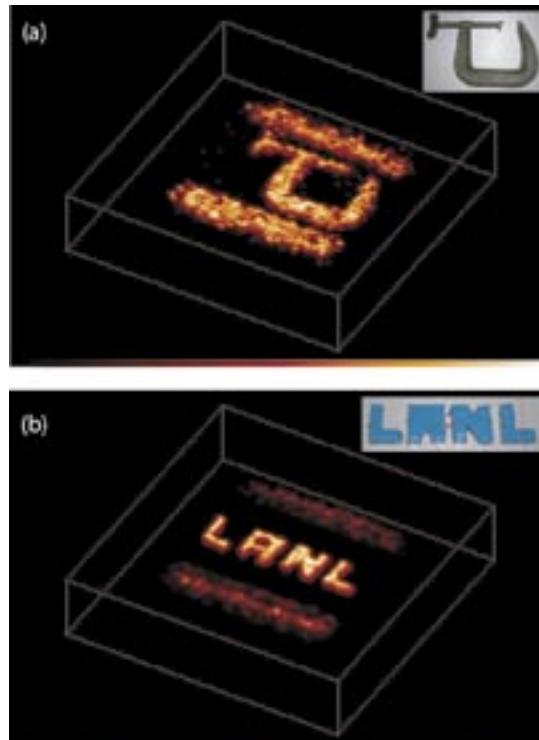


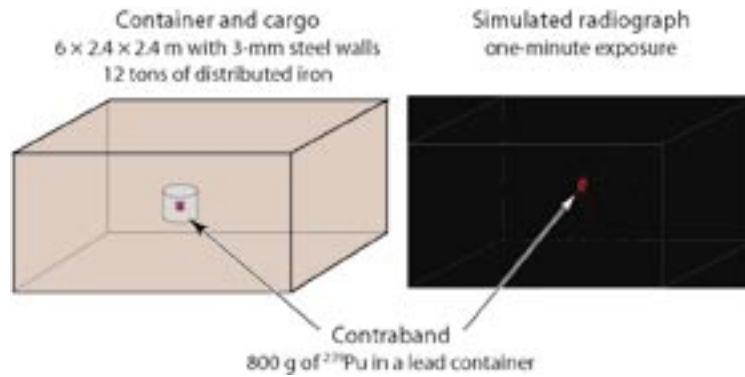
Figure 3. The scattering of muons passing through material varies strongly with the Z number of the material.

Figure 4. Experimentally produced cosmic-ray muon radiographs of (a) a steel c-clamp and (b) the acronym "LANL" constructed from 1-in.-lead stock. The bar-like features visible on either side of the images result from steel beams used to support a plastic object platform.



## Instrumentation Research Highlights

Figure 5. Simulation of a steel-cargo container with SNM contraband buried within iron (left) and a one-minute cosmic-ray muon radiograph (right).



### Conclusion

We have developed and experimentally demonstrated a unique radiography method using the multiple-scattering process of cosmic-ray muons. This method, which is particularly sensitive to high-Z dense materials, may prove useful in detecting smuggled cargoes of SNM in incoming vehicles and commercial traffic at U.S. borders in short times with no additional radiation dose to vehicle occupants or border guards. Our current efforts are devoted to confirming our small-scale experimental and full-scale simulated results with a full-scale experimental demonstration; to developing low-cost, field-deployable detectors; and to optimizing our information-processing methods.

### References

1. L.W. Alvarez *et al.*, "Search for hidden chambers in the pyramids," *Science* **167**, 832-839 (1970).

### Acknowledgment

The researchers acknowledge LANSCE at LANL for providing legacy equipment used in the muon-radiography experiments. We also acknowledge the diligent work of the P-25 technician team. Finally, we acknowledge our collaborators in NIS Division and Gary Blanpied from the University of South Carolina. This work was sponsored by the Office of Nonproliferation Research and Engineering of the DOE NNSA.

For more information, contact Larry Schultz, 505-667-9431, [schultz@lanl.gov](mailto:schultz@lanl.gov).



Electron beam measurements are being performed in support of DARHT-II accelerator operation. These experiments fall into two separate categories: (1) investigating beam-target interaction and (2) measuring time-dependent electron beam energy.

The beam-target interaction studies are performed using the DARHT-I accelerator where a 60-ns-long, 19.8-MeV, 1.7-kA electron pulse is passed through a thin foil. The electron beam has been found to thermally desorb neutral gas species from the foil/target surface that are then subsequently ionized by beam electrons. These ions are trapped in the beam potential thereby generating a time-dependent positive charge density within the electron beam. Interaction between the beam electrons and these ions causes the beam focal point to change as a function of time and results in an effective increase in radiographic spot size. Techniques are currently being investigated to minimize the neutral/ion generation from the radiographic target because DARHT-II will generate four electron pulses ranging up to ~ 400 ns in duration.

The DARHT-II electron beam energy is being measured as part of the accelerator-commissioning activities using a magnetic-sector-electron spectrometer. The technique uses a streak camera to measure the time-dependent beam deflection due to the magnetic field of the spectrometer. The electron energy is then calculated as a function of time using both the magnetic-field strength and electron-deflection distance. This information is used to both diagnose the accelerator performance and define the DARHT-II radiation spectrum.

The three-year Enhanced Test Readiness (ETR) program, sponsored by the NNSA, will shorten the time between the authorization of an underground nuclear test and its execution from the current three years to eighteen months. The ETR program covers a broad range of activities related to underground testing; however, P-21, in collaboration with P-22, is involved in the reaction-history component of the program. A critical component involves passing on knowledge from experienced scientists and diagnostics engineers, who are mostly now retired, to a new group of scientists and engineers too young to have participated in the last underground test in 1992. We are now calibrating and testing equipment that has not been operated since the end of underground nuclear tests. For example, the “digital alpha” reaction-history diagnostic (Figure 1) has been partially resurrected—its hardware is being tested, and its software is being upgraded to modern programming languages and computer platforms.

New methods of recording reaction history are being considered. These methods are often driven by the fact that we have lost the capability to support equipment historically used in routine procedures. The old Rossi oscilloscopes, for example, are available, but we cannot manufacture new ones. Fast transient recorders like the Tektronix SCD-5000 are no longer available. New products from commercial vendors, primarily developed for the communications industry, are designed under a vastly different set of requirements than those that we have for reaction history. Specialized cables and interconnect, which were developed during the active underground testing program, are no longer manufactured. Our challenge is to apply new technology and techniques and to integrate them with traditional experience and resurrected equipment in such a way that weapons designers will not notice the difference in test data between a future underground test and one performed twelve years ago.

### Physics Measurements for DARHT-II Optimization and Risk Mitigation

*R.T. Olson (P-22), D.M. Oró (P-22), H.A. Davis (DX-6), D.C. Moir (DX-6)*

### Enhanced Test Readiness— Sub-Nanosecond Time Domain Electronics Enhanced Test Readiness Program

*J.M. Galbraith, S.K. Wilson, E.Y. Raby, J.D. Moses (P-21)*



Figure 1. Archival photo of the “digital alpha channel” used in experiments at NTS.

## Instrumentation Project Descriptions

### DynEx Confinement Vessel, Shipping Structure, and Cover-Installation Fixture

*E.O. Ballard (P-22), C. Romero (DX-5), D.H. Bultman (ARES Corporation)*

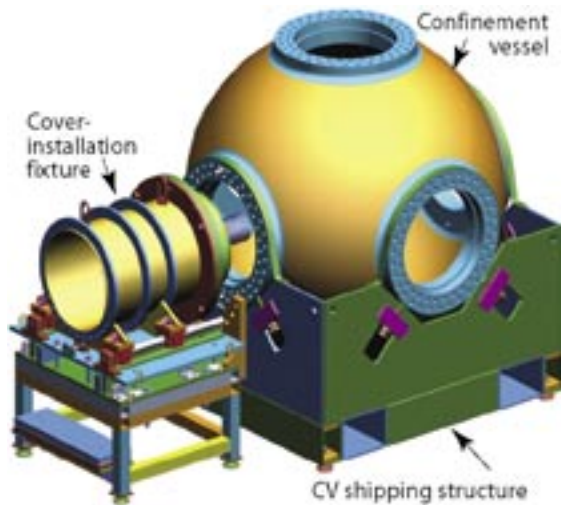


Figure 2. DynEx confinement vessel, shipping structure, and cover-installation fixture.

The DynEx confinement vessel (Figure 2) will be used to contain the energy, debris, and combustion gases from detonation of a high-explosive experiment. The vessel will enable real-time radiographic imaging of the detonation by providing radiographic “windows” integral to flange covers on the nozzle openings. Through these windows, x-rays can enter and exit the vessel boundaries and project onto x-ray scintillator panels outside the vessel, thereby producing visible images. These images are recorded using CCD cameras. The capability for x-ray imaging through the vessel in this manner will be provided along two perpendicular, co-planar axes, which pass through the center of the spherical confinement vessel. Radiographic hardware will be mounted inside the confinement vessel, along with the experiment package, to collimate the x-rays onto the experiment and to support and align the experiment relative to the x-ray sources. Other components mounted in the vessel will mitigate the effect of fragments impacting the vessel wall.

During operation, the confinement vessel will be positioned and supported inside a larger safety vessel, which will serve as a secondary pressure boundary to contain the high-explosive detonation in case of a confinement vessel breach. Flexible piping will connect the two vessels with an in-line, remotely operated valve to permit vacuum pump-down of the confinement vessel before an experiment and followed by ventilation with filtration after the experiment.

Ancillary hardware includes the shipping structure and cover-installation fixture. The shipping structure is also used for hydrostatic testing of the vessel and storage at LANL. The cover-installation fixture enables handling of the heavy radiographic covers during the process of the experiment buildup and alignment.

### HPGe-Based Handheld Radioisotope Identification Instrument

*C.M. Frankle (P-22), K.B. Butterfield, W.S. Murray, B.A. Sapp, S.A. Salazar (N-2), J.A. Becker, J. Collins, C.P. Cork, L. Fabris, N.W. Madden (Lawrence Livermore National Laboratory)*

LANL has a long and successful history of fielding handheld radioisotope identification instruments. Such instruments use gamma-ray spectroscopy to identify isotopes of interest. Early instruments were based on sodium iodide [NaI(Tl)]. NaI(Tl) has good efficiency and can be made quite rugged. However, it suffers from relatively poor energy resolution ( $dE/E \sim 7\%–9\%$ ). This makes the identification of isotopes that emit gamma rays of similar energy very difficult—particularly in an automated manner in a handheld instrument intended for an unsophisticated user. A potential improvement is through the use of cadmium zinc telluride (CZT), which has better energy resolution ( $dE/E \sim 1\%–2\%$ ). The difficulty with CZT is that detector-grade crystals can only be fabricated in rather small sizes ( $\sim 1–2 \text{ cm}^3$ ), which means a very low efficiency. The gold standard for isotope identification is the use of high-purity germanium (HPGe) with an energy resolution of  $dE/E \sim 0.1\%–0.2\%$ . However, HPGe requires cooling to near liquid-nitrogen temperatures (77 K) in order to achieve that resolution, and HPGe detectors also tend to be quite fragile. Liquid nitrogen and its support systems are clearly not compatible with a handheld instrument.

Approximately five years ago, our collaborators at LLNL were successful in attaching a modest-size HPGe crystal to a fairly low-power ( $\sim 10 \text{ W}$ ) mechanical cooler. We then provided them with a basic design for a detector head that would have an efficiency similar to our existing NaI(Tl)-based instruments and would be suitable for use in a handheld instrument. The result of the collaboration of the HPGe-detector-fabrication expertise of

LLNL with LANL instrument-design expertise is an instrument named GN-5. The GN-5 contains a mechanically cooled HPGe detector (using a mere 3-W average power at room temperature), a bismuth germanate (BGO) Compton suppression shield, and two neutron detectors. This capability is packaged in a rugged, rain-tight case with the simple, push-button operation characteristic of all the GN-series instruments. Deployment of the first units to U.S. government customers is slated for early 2004.

P-22 has a representative on the Interdivisional Red Team (team members include representatives from X, T, MST, C, D, DX, and P Divisions), which is tasked with providing peer review to the W88 Core team. We have been collecting information and reviewing how experimental results have been and can be used in the certification process. An important part of this work is to try to determine the value that future experiments may provide to the certification process and help select the most promising experiments.

Members of P-25, N-2, and ISR-2 are working on a concept that will significantly improve the sensitivity of detectors used for remote sensing of radioactive materials using advanced Compton gamma-ray imaging. This type of imaging can localize gamma rays from radioactive nuclear materials and therefore allow us to distinguish them from background and identify their unique isotopic composition. The technique is important for homeland defense, astrophysics, and medical imaging. Compton scattering is the scattering of a gamma ray from an electron. By accurately measuring the angle and energy of the scattered gamma and the electron it scattered from, the direction of the incoming gamma ray can be calculated with a simple formula. If only the energy of the electron (not its angle) is measured (which frequently happens), the direction of the incoming gamma ray is not determined exactly, but the direction of the cones of light from the Compton scattering can be calculated from the same formulas. In either case, an image is built up from either the vectors (if the electron angle is measured) or the light cones (if not) from many gamma rays. The location of the source or sources can be determined from this image.

In the last year, we developed a prototype detector system, which was designed so that gamma rays could Compton scatter in one of three layers of 300- $\mu$ m-thick Si-pixel detectors (Figure 3). The scattered gamma rays are then absorbed by one of 42 CsI detectors where they are detected. Each of the three planes of Si-pixel detectors has a sensitive area of 48 x 60 mm, which is divided into 320 pixels, each 3 x 3 mm. We also purchased and tested readout electronics (based on commercially available application-specific integrated circuits) for each pixel (960 total). The electronic noise from both the Si-pixel detectors and the readout system was measured and found to be about 2.6 keV (root mean square). Each of the 42 CsI detectors is approximately 12 x 14 x 10 mm and is attached to a photodiode used in fiber networks followed by a preamplifier. The individual crystals were tested and found to have a typical resolution of approximately 47 keV (root mean square), which we are attempting to improve. The next steps will be to integrate the Si- and CsI-detector readout systems and then to produce and compare images of real sources to our extensive Monte Carlo simulations of the system. Our longer-term goal is to build a real device that will be much larger than the prototype system; we hope to replace the CsI detectors with a higher-resolution detector in this larger device.

### W88 Pit Certification Red Team

*B.J. Warthen (P-22), representing the Interdivisional Red Team*

### Compton Gamma-Ray Imaging for High-Sensitivity Detection of Nuclear Materials

*J.P. Sullivan (P-25), G.J. Arnone (N-2), D.K. Hayes (N-2), A.S. Hoover (ISR-2), R.M. Kippen (ISR-2), M.W. Rawool-Sullivan (N-2)*

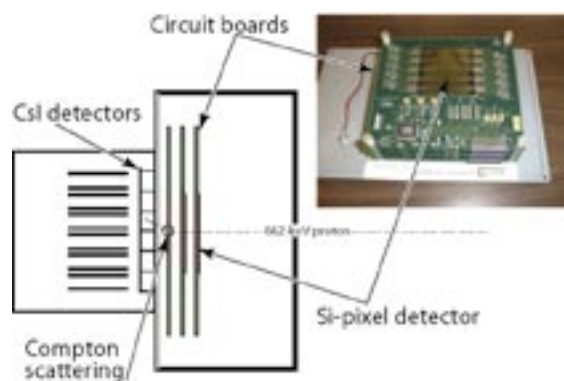


Figure 3. This cross section of the detector system shows the CsI detectors as small rectangles marked by an arrow. A 662-keV photon enters the system from the right, Compton scatters in the third Si-pixel detector, and is absorbed in one of the 42 CsI detectors. The electron (not seen in the figure) resulting from the Compton-scattering event remains in the Si-pixel detector where it was produced. The inset is a photo of the Si-pixel detectors.



## Instrumentation Project Descriptions

### High-Definition Television

G.H. Nickel, E. Stauffer, F.J. Wysocki (P-22)

Members of P-22 are developing methods of encoding information to deliver digital TV images using the “NTSC” (National Television System Committee) signal format used by existing analog television sets—the image data for HDTV can also be viewed by analog TV receivers. No hardware modifications are required for the old monitors or the new high-definition sets.

In the scheme described here, the information for the digital images (quantized coefficients in the transform space) is transmitted by modulating the carrier in a novel way. The coefficients are computed for  $8 \times 8$  pixel blocks, as in the current standard, and partitioned into subsets according to the spatial resolution. Our scheme selects low-order coefficients in accordance with the relative bandwidths for the luminance and chrominance components of the video signal to generate the compatible image for the NTSC format. Because these coefficients must appear as an image in the coefficients of analog receivers, they cannot be entropy coded. Instead, they are transformed directly from their digital form back to the image space and transmitted as a “digitally mastered composite video” waveform using amplitude modulation. This transformation is designed to create an image in analog receivers and provide for the recovery of the original discrete data by inversion, without introducing extra sensitivity to signal noise. The remaining “high-order” digital information can be partitioned again, if desired, and transmitted in such a way that it is invisible on analog receivers but recoverable by digital sampling. This information is compressed using entropy coding and offers a compression advantage.

Our research team assembled a demonstration prototype using these principles and commercial off-the-shelf hardware. We used computers with added signal processors and analog-to-digital converters to create the required waveforms and act as HDTV decoders. With further development, it will be possible to apply existing results from information theory and digital-modulation techniques to avoid duplication of television-channel programming (required under the current official transition plan) during the national transition to high-definition content.

### Laser-Based High-Resolution, High-Energy X-ray Imaging of High-Energy-Density Targets Using a Backlit Pinhole

J. Workman, J. Fincke, G. Kyrala (P-24), T. Pierce (MST-7)

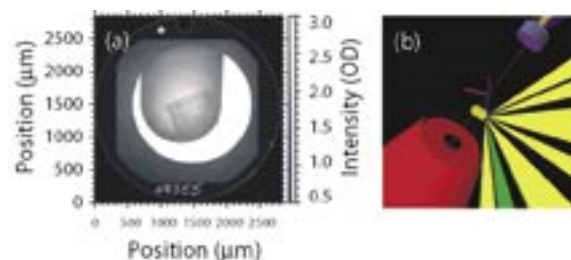


Figure 4. (a) A static x-ray radiograph at 9 keV of a hohlraum on the Omega laser. A  $62\text{-}\mu\text{m}$  ( $20\text{-}\mu\text{m}$  bar width) period grid was used for spatial calibration. (b) Configuration showing diagnostic nose tip, hohlraum, and backlighter substrate.

In P-24, we have demonstrated a new x-ray backlighting technique at 9 keV that produces uniform, large-area, monochromatic, high-resolution images of targets used for laser-driven above-ground experiments (AGEX) and HED physics experiments. X-ray imaging at moderate energy in laser-driven HED physics experiments is an essential, well-established tool for observing dynamic phenomena such as shock trajectories, interface motion, and instability growth. However, the standard technique using an area back lighter, the size of the object to be radiographed, requires an inordinate amount of laser energy to produce a monochromatic x-ray source above 7 keV. Figure 4(a) shows the raw image of a thin-walled gold hohlraum used for radiation-driven experiments recorded on x-ray film using the backlit-pinhole technique. Figure 4(b) shows the hohlraum in the center with 12 laser beams “driving” it. The top right corner of Figure 4(b) shows the backlighter substrate, whereas the red object is the opening of the diagnostic camera. Signal-level improvements over the standard-area backlighting technique have been increased by greater than a factor of 65. This is an important diagnostic development that was driven by requirements for higher-energy x-ray backlighting in current experiments on the Z accelerator at SNL, the Omega laser at the University of Rochester, and future experiments on NIF.

The Precision High Energy Liner Implosion Experiment (PHELIX) is an LDRD concept venture that uses the advantage of the turns-ratio of a common transformer design to produce high currents—for use in magnetically driven, hydrodynamic liner experiments. The advantage of this approach (to isolate the experimental fixture from a driver capacitor bank) lends itself to the possibility of application to the pRad “photographic” capabilities at LANSCE. The pRad facility has proven its capability to produce multiframe (20 frames/ $\sim 30 \mu\text{s}$ ) radiographic data of dynamic experiments. The confines of the pRad beam-line area require the use of a compact system—in contrast to a facility like Pegasus II or Atlas where users bring compact x-ray sources to the machine to record experimental data. Here, users bring the hydro-driver/experiment assembly (PHELIX) to the diagnostic, data-gathering device (pRad).

A toroidal design, PHELIX uses a multiturn primary winding that is fed electrical energy from a compact capacitor bank (via an array of coaxial cables, similar to Atlas’ maintenance-unit design) and a single-turn secondary that feeds the transformed current into a central experiment/liner assembly. The toroidal layout is such that the driven liner becomes part of the secondary—minimizing resistive and inductive losses typical of the power-flow channel in similar hydrodynamic/magnetic drivers. The inductive and resistive portion of the circuit is shifted to a higher-impedance side of the network, reducing the loss. This combination of mechanical and electrical design can facilitate either radial or axial pRad of the experiment core by simply rotating the transformer in the beam line. The capacitor bank uses capacitors and rail-type spark gaps developed for Atlas in a compact, oil-filled unit that can roll (on tracks) in and out of the beam line for maintenance and loading experimental apparatus. A prototype transformer was constructed and tested in spring 2003 with promising results. A test and development facility is now being assembled at TA-35 to push the design to a “first-article” test with a target-test-shot date of December 2003 for proof of principle. An attempt at a test liner compression should follow in early 2004.

Several hydrotests were recently performed at the PHERMEX radiographic facility to examine radiation case dynamics under high-explosive loading. A low-energy, multi-frame x-ray system was also fielded to provide a second line of sight perpendicular to the PHERMEX beam axis. This x-ray system consists of four x-ray heads (each driven by a 900-kV Marx bank) that share a nearly identical line of sight. The x-ray radiographs were recorded on a CCD coupled to an electronic framing camera that images an LSO (cerium-doped lutetium oxyorthosilicate) scintillator via a 6-m-long optical path. The four x-ray heads were timed to provide images before, between, and after the two PHERMEX radiographs. All the equipment, with the exception of the camera and Marx banks, was destroyed during the experiments because of its proximity to the high-explosive charge.

### **The PHELIX “Transformer” for Proton Radiography Hydrodynamics**

*W.B. Hinckley, J.E. Martinez, M.C. Thompson (P-22),  
F. Venneri (LANSCE-3), P.J. Turchi (Phillips Laboratory, U.S.  
Air Force)*

### **Low-Energy X-ray Radiography of Hydrotest Case Dynamics**

*R.T. Olson, D.M. Oró, D.T. Westley, A.M. Montoya,  
B.G. Anderson (P-22)*

## Instrumentation Project Descriptions

### Cygnus Radiographic X-ray Source

*J.R. Smith, R.L. Carlson (P-22), R.D. Fulton (P-23), E.A. Rose (DX-3), R. J. Comisso, G. Cooperstein (Naval Research Laboratory), V. Carboni, D.L. Johnson, I. Smith (Titan Pulse Sciences Division), D. Droemer, D.J. Henderson (Bechtel Nevada), J.E. Maenchen (Sandia National Laboratories)*

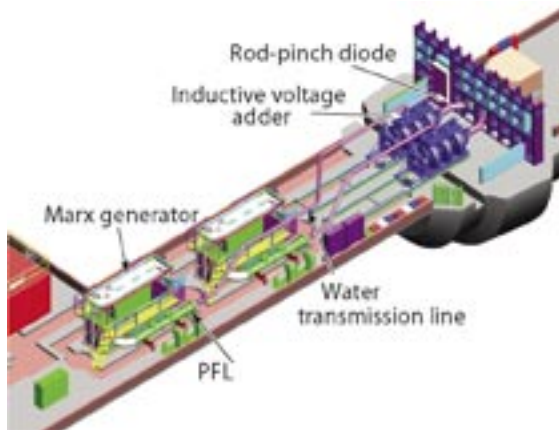


Figure 5. Two Cygnus x-ray sources located downhole at the NTS U1a complex.

Cygnus is a radiographic x-ray source developed for support of the SCE program at NTS. Its architecture, which is scalable, contains the most complex and largest hardware components ever deployed as a diagnostic for underground installation at NTS. Major features of the Cygnus source are a dramatically reduced spot size (as compared to existing alternatives), layout flexibility, and reliability. Cygnus incorporates proven pulsed-power technology (Marx generator, PFL, water transmission line, and inductive voltage adder subcomponents) to drive a high-voltage vacuum diode. In the case of Cygnus, a relatively new approach, the rod pinch diode, is employed to achieve a small source diameter. Cygnus has met the following design specifications: 2.25-MeV endpoint energy, 1.2-mm source diameter, and 4-rads dose at a distance of 1 m. Its reliability has been demonstrated at LANL in a test series that incorporated more than 300 shots. A notable requirement for operation downhole at NTS is a remote, computer-based control and monitoring system, which has also been developed and fielded.

The first application of the Cygnus radiographic source is the Armando SCE, scheduled in 2004, which will be fielded to study the dynamic properties of plutonium. Two Cygnus sources have been manufactured, integrated, and successfully tested as the prime diagnostic for this experiment (Figure 5). They will be configured to give two radiographic images with different views and at different times. The test object will be contained in a vessel thereby permitting reuse of the facility. The new and improved features offered by the Cygnus radiographic source greatly enhance the diagnostic capability for the SCE program at NTS.

### Advanced Plasma Diagnostic Concepts for National Magnetic Fusion Energy Research

*G.A. Wurden, Z. Wang, J. Park (P-24)*

We have been working on a new plasma diagnostic to measure the internal magnetic fields in today's generation of research plasmas. We propose to develop a hypervelocity dust beam (micron-sized dust traveling at  $\sim 10$  km/s) to inject a source of neutrals deep into the National Spherical Torus Experiment spherical tokamak plasma at Princeton University. By taking snapshots of the dust beam (from a tangential view) using high-resolution cameras, we can observe the small "comet-like" tails of the ablating dust particle. Their orientation will give us the direction of the local magnetic field inside of the plasma. This type of information would be of great help in many alternate plasma configurations where the internal magnetic fields (when the plasma is present) are quite different than the original vacuum magnetic fields (when the plasma is absent).

For tomorrow's high-performance fusion tokamak machine—the International Thermonuclear Experimental Reactor, we have been working on restarting a project originally developed at LANL about 15 years ago. That project had as its goal the development of an extremely bright, pulsed, intense diagnostic neutral beam. This atomic beam of hydrogen (or helium), operating at a voltage of  $\sim 100$  keV/AMU, at a current of 10 kA in 1- $\mu$ s pulses, and at a 10- to 30-Hz repetition rate, will provide a source of neutrals for spectroscopy purposes. Without this source, there are no neutrals normally present deep inside the core of the fusing tokamak plasma. With this source, profiles of plasma-ion temperature, helium-ash buildup, and the plasma-current profile can all be obtained by analyzing light emitted from the neutral atoms in the beam.



## Instrumentation Project Descriptions

### 40-mm, Gunpowder Breech Launcher for Proton Radiography Experiments

*E.O. Ballard (P-22), P.A. Rigg, D.L. Shampine (DX-2)*

A 40-mm bore, powder-breech launcher was designed, fabricated, assembled, and tested for use at the LANSCE pRad facility (Figure 6). The 40-mm launcher is an experimental device to be used for determining EOS and metallurgical properties of materials under extreme dynamic-loading conditions in real time. The launcher system consists of a 40-mm smooth-bore launch tube (barrel), a propellant breech, and an enclosed target-chamber and catch-tank assembly. The launch tube/breech assembly measures approximately 11.5 ft in length and rests on bronze bushings at two contact points. The muzzle end of the launch tube is located inside the target chamber, and the entrance point to the chamber is sealed using an O-ring slip seal. Launch-tube recoil is limited to 4 in. of travel by using two industrial shock absorbers, which retain the muzzle of the launch tube inside the target chamber after the shot. Because the only contact between the launch tube and target chamber is through the slip seal, the momentum transferred to the target chamber caused by recoil of the launch tube is negligible. The entire assembly is attached to a platform on rails set perpendicular to the proton beam line in such a way that the target chamber can be aligned and mounted to the beam line. The target chamber and catch-tank contain the projectile and combustion gases from the propellant. The beam-tube volume is also used for containing propellant gases.

The target assembly is located at the muzzle end of the launch tube inside the target chamber and consists of the material of interest for the experiment and various diagnostic electrical pins and optical probes. The projectile consists of a main body comprised of various materials in mass less than or equal to aluminum. Projectile materials include, but are not limited to, Lexan® (polycarbonate), aluminum, or magnesium and weigh from 100 to 500 g. A thin impactor (typically metal but ranging from plastics to single-crystal sapphire) is glued to the front of the projectile for direct impact with the target material. At least one O-ring is included at the rear part of the projectile to serve as a vacuum seal. A thin phenolic shear disk is placed on the back of the projectile to hold it in place until the launcher is fired. The projectile assembly is accelerated down the launch tube using up to 300 g of a Class 1.3 smokeless gunpowder at a velocity to 2 km/s. The projectile (or, more specifically, the impactor) then impacts the target, at which point the experimental measurements take place. A series of seven hanging catch-plates located in the catch-tank then stops the projectile and target shrapnel produced by the impact.

A variety of diagnostic tools can be employed, including pin circuits to examine wave-propagation times, laser interferometry and spectroscopy, CCD cameras, temperature probes, and oscilloscopes.

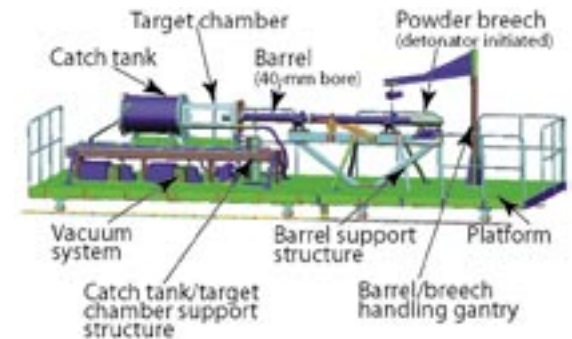


Figure 6. The 44-mm gunpowder breech launcher for pRad experiments.

VISAR is an important diagnostic that can provide detailed surface-velocity information for pRad experiments in Area C at LANSCE. P-22 has constructed a VISAR system for pRad and provides support to field experiments that use VISAR. In addition, we provide support for general pRad beam operations. Experimental support includes design and installation of VISAR equipment, data acquisition, fiber-optic and coaxial cable plant, safety documentation, experiment documentation, data analysis, and mechanical-technician help.

### VISAR at pRad

*D.A. Clark, O.F. Garcia, B.J. Hollander (P-22), D. Tupa, (P-25)*

## Instrumentation Project Descriptions

### Thermonuclear Burn Physics Using High-Energy Fusion Gamma Rays

*J.M. Mack, D. Esquibel, S.C. Evans, R.S. King, D.K. Lash, J.A. Oertel (P-24), S.E. Caldwell, C.S. Young (P-22), R.R. Berggren (ISR-2), J.R. Faulkner, Jr. (DX-3), R.L. Griffith, R.A. Lerche (Lawrence Livermore National Laboratory)*

As fusion ignition conditions are approached using NIF, independent, high-bandwidth, gamma-ray fusion-burn measurements become essential complements to neutron-based diagnostic methods. Time resolution,  $\sim 20$  ps (10–30 GHz), energy discrimination, and significant stand-off distance may be needed for credible burn-history measurements. The idea of using high-energy fusion gamma rays for burn-history evaluation was conceived and pursued as part of the downhole test program at NTS more than two decades ago. With potent fusion sources now available on the Omega laser at the University of Rochester and with upcoming availability at NIF, this possibility exists once again and is being vigorously pursued by a multi-institution collaboration led by P Division, including the key original NTS personnel.

The 16.75-MeV gamma rays that accompany DT fusion provide a high-bandwidth alternative to 14-MeV fusion neutrons for DT burn-history measurements. Fusion of deuterium with tritium produces an excited  $^5\text{He}$  nucleus, which then has several possible de-excitation modes. The most common mode emits a 14-MeV neutron and a 3.5-MeV alpha particle. Much less frequent gamma-ray modes emit gamma rays at 16.75 MeV to the ground state and possibly at  $\sim 12$  MeV to a broad level near 4 MeV. Recent values for the DT branching ratio (16.75-MeV gamma rays per 14-MeV neutron) vary from  $5 \times 10^{-5}$  to  $1 \times 10^{-4}$ . Because of this unfavorable branching ratio, high-yield DT implosions ( $> 10^{12}$  neutrons) are required to provide high-energy gamma-ray output of sufficient strength for a credible measurement.

A thresholding detector, based on the Cerenkov effect, resulting from Compton and pair-production electron interactions in gaseous carbon dioxide, offers a means of separating the high-energy fusion gamma rays from other background sources (Figure 7). When coupled to appropriate streak-camera recorders, a gas-Cerenkov-detector (GCD) system response to 20 GHz is feasible. Initially, as a proof of principle, a GCD system employing a 1-GHz photodiode detector was successfully fielded at the Omega laser facility. A comparable system was also operated with a streak camera replacing the photodiode detector, thus allowing similar measurements to be made at higher bandwidth ( $\sim 15$  GHz). High-energy fusion gamma-ray measurements have been made on a number of DT capsule implosions, which have had neutron outputs ranging from  $1 \times 10^{12}$  to  $8 \times 10^{13}$  neutrons. For the first time, using ICF implosions, high-energy fusion gamma-ray signals were unambiguously observed with both instruments at Omega. These results have established the feasibility and utility of high-bandwidth GCD-based, high-energy DT fusion-burn gamma-ray measurements for acquiring burn histories using laser-driven implosions. This new diagnostic method is now approved as a future diagnostic package for NIF.

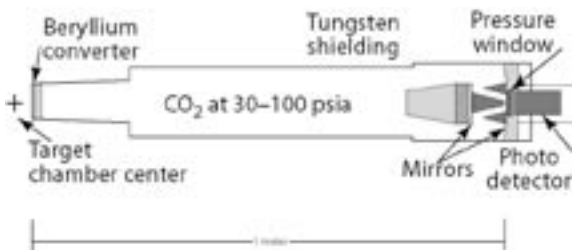


Figure 7. GCD system as configured for insertion into the evacuated Omega laser target chamber. Sixty converging laser beams implode the DT targets placed at the target-chamber center.

### KEYPATH: Using Atmospheric Turbulence to Generate and Exchange a Cryptographic Key

*G.H. Nickel (P-22), S. Xie (University of Texas, Dallas)*

When a laser beam is transmitted through turbulent air, the eddies create time-dependent temperature differences, which in turn cause density variations. If the beam diameter is not too large (several centimeters), the perturbations caused by these variations are simply “tilts” of plane of constant phase and can be shown to be truly random with a correlation time of a few milliseconds. Such “tilts” are easily measured by determining the change in position of the resulting spot in the focal plane of an optical system. Perhaps surprisingly, when two beams are propagated along the same path in opposite directions, measurements at each end of the path demonstrate a high

correlation. Therefore, observations of these “tilts” can be used to generate random sequences, which are the same for both observers. Because this random sequence depends on the particular air column between the observers, it is also secure from measurement by a third observer unless the exact path is traversed. Thus, the sequences are random, correlated, and secure; these are the conditions for the exchange of a cryptographic key. The security of this scheme is due to the impossibility of modeling turbulence exactly.

A demonstration of the effectiveness of this system, called KEYPATH, is under development. Shumao Xie, a graduate student at the University of Texas at Dallas, and George Nickel, a staff member in P-22, have been taking measurements over paths of varying lengths and demonstrating the correlation. To date, paths of 100 m have yielded over 90% correlation in the resulting bit streams, and greater path lengths are being considered. The only fundamental limitation to the length comes from the condition that the turbulence should not change during the time for the light to transit the path. The characteristic correlation time has been measured to be 10 ms, meaning that 100 independent bits of key can be generated each second—and that paths of many kilometers are possible.

Shumao Xie will continue this work as his Ph.D. thesis at the University of Texas, and George Nickel is working with ISR Division to extend the concept to an analogous situation involving transmission of radio signals in the earth’s magnetosphere. The work has been approved for patent application.

The objective of these experiments was to determine the radial-wall displacement of a DynEx containment vessel (Figure 8) during detonation of different high-explosive loading conditions. The data from these experiments and the strain-gauge measurements of the containment vessel’s outer surface verify models of vessel behavior. Two types of experiments, mitigated and unmitigated are performed, both of which were conducted at atmospheric pressure. The mitigated experiments use glass balls in the vessel to lessen the shock effects created by the high-explosive pressure wave, whereas the unmitigated experiments simply consisted of a spherical high-explosive charge hanging in an empty vessel. All experiments were configured with spherical PBX-9501, which was centrally detonated with one ER-453 detonator. The high-explosive charges were held in place with a specially designed sling, centering the charge in the vessel to within  $\pm 1$  mm.

Microwave interferometers are used to measure displacement of the vessel walls as a function of time. The system uses a pair of microwave interferometers—one with a 24-GHz fundamental frequency and one with a 94-GHz fundamental frequency. A feed horn is used to both emit and collect a signal that is reflected off the surface of the vessel. The reflected signal is amplified, split, and interfered in quadrature with the reference leg of the interferometer. Two detectors record the intensity variation of the interfered signals as a function of time. The phase change and the known wavelength of the system are used to determine the displacement of the outer surface of the vessel. The unmitigated-experiment data indicate initial vessel-wall expansion, as well as vessel motion approaching that of a simple harmonic oscillator with a defined, repeatable period. The mitigated-experiment data indicate that the vessel wall initially expanded on one side and contracted on the other. The oscillations indicate a difference in time between the initial motion and the amplitude of motion as directly proportional to the high-explosive loading.

### Interferometer Displacement Measurements of DynEx Vessel Oscillations

*D.T. Westley, R.T. Olson, J.K. Studebaker, D.A. Clark, B.G. Anderson, A.M. Montoya, B.N. Vigil, J.C. Armijo (P-22)*

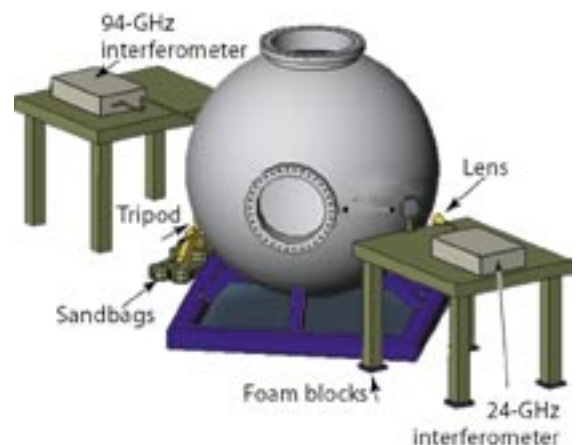


Figure 8. Diagnostic layout of 6-ft-diam DynEx containment vessel and microwave interferometer systems.



## Instrumentation Project Descriptions

### Advanced Detectors for Proton Radiography—Raising the Bar in Ultra-Fast Imaging

K. Kwiatkowski, N.S.P. King (P-23), C. Morris (P-25), M. Wilke (P-23), S. Kleinfelder (UC-Irvine), J. Lyke (Air Force Research Laboratory), V. Douance, P.O. Pettersson (Rockwell Scientific), R. Wojnarowski (General Electric-Global Research)

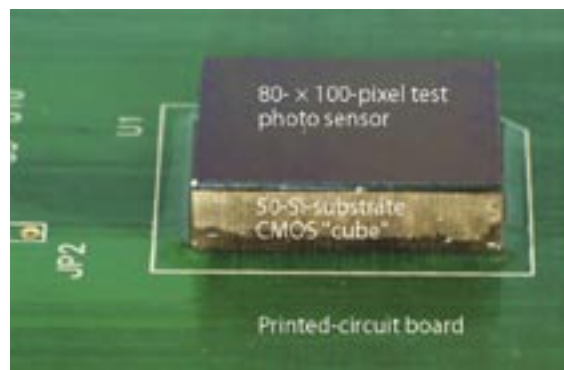


Figure 9. Imaging cube assembly—50 double-density chips stacked on edge with an 80- x 100-pixel test photo sensor that is bump-bonded to the top of the cube.

The invention of pRad has opened new opportunities in flash radiography. The combination of pRad's multiple-frame ( $\sim 50$ ), high-penetrating-power, high-speed, and high-resolution capabilities has made this unique technique a powerful tool in quantitative studies of fast transient phenomena evolving on sub-microsecond timescales. However, pRad has also imposed great demands on the optical imagers used in the experiments. We are developing new detectors to replace the current “seven-shooter” gated CCD camera system. The interim solution is based on a back-illuminated hybrid CMOS (complementary metal oxide semiconductor) imager. This 2-mega-pixel camera, which is being built at Rockwell Scientific, operates in a burst mode. It can acquire three frames spaced 300 ns apart and provides about a 100% fill factor, high quantum efficiency, and a large dynamic range of 11 bits. In parallel, we are developing enabling technologies (sensors, CMOS electronics, and interconnect technology) for an instrument that can fully meet the challenges of high-resolution, multiple-frame pRad. The construction of a mega-pixel, 64-frame, fast-imaging system is complicated by the tremendous requirements on the data-recording bandwidth and by equally severe demands on the instantaneous power that has to be delivered to the front-end electronics and to the sensor during the acquisition time. One approach to reconcile the opposing demands for smaller, denser pixels and greater functionality is to stack the signal-processing electronic chips, like a deck of playing cards, into a three-dimensional cube structure, which can be placed directly below a photo-sensor array. This approach can increase the available pixel silicon area by a factor of 20 to 100. The proof-of-concept cube was recently fabricated in a collaborative effort with General Electric-Global Research Center using test/continuity silicon chips (Figure 9).

Concurrently with the development of the interconnect technology, we have made strides in the design and fabrication of custom CMOS electronics that can deliver the required electrical performance for the 64-frame imager and can be laid out in  $< 50\text{-}\mu\text{m}$ -wide “channels.” We designed and tested an integrated-circuit prototype, as a  $12 \times 12$  CMOS focal plane array, that acquires images at a rate of 4 mega-frames per second with over a 79-dB, or 13-bit, dynamic range. The  $200\text{-} \times 200\text{-}\mu\text{m}^2$  pixels were equipped with a small photodiode, a charge-integrating amplifier, a direct-integration source follower, 64 frames of *in situ* storage via an array of sample and hold capacitors, and output multiplexing circuitry. The chip can perform either correlated double sampling (recording 32 frames at 4 mega-frames per second) or single sampling (64 frames at 7 mega-frames per second). Additionally, we designed and tested a solid state CMOS “streak camera.” This camera performed up to a 400-MHz (2.5-ns) electrical test and over 100 MHz using optical stimulation with more than 10 bits of dynamic range. The prototype contained a one-dimensional array of 150 photodiodes, each with 150 frames of storage. Using three-dimensional packaging techniques, the streak-camera concept can be leveraged to create an ultra-fast camera system capable of capturing images at tens of tera-pixels per second. For example, a common-interchange-format ( $352 \times 288$  pixels) imager with a storage capacity for 1,024 frames is feasible. When it is run at 200 MHz, it will acquire over 100 megabytes of image data in 5  $\mu\text{s}$  at the effective speed of over 20 terabytes per second (i.e.,  $20 \times 10^{12}$  bytes per second).

### Reaction-History Reanalysis

*B.J. Warthen (P-22), representing the Reaction-History Reanalysis Team*

The reaction-history measurement is a high dynamic-range measurement of gamma rays and was usually made during each underground nuclear event at NTS. On each event, the reaction-history measurement involved several detectors—each requiring several data-recording channels to cover the detectors' dynamic range. Most often, a data-recording channel consisted of a Rossi oscilloscope that produced a vertical deflection proportional to the gamma-ray flux and a horizontal deflection proportional to a sinusoidal time-base. The trace of each Rossi oscilloscope was recorded on film. An example of a very clean Rossi trace film (simulated) is shown in Figure 10.

After an NTS event, the films were hand-digitized to produce (x,y) data points that represent the traces; the data points were used to calculate the flux as a function of time, and the flux functions from each of the channels of a detector were combined together to produce a composite flux curve for the detector. The alpha curve was produced by calculating the logarithmic derivative of the flux curve and then applying an adaptive Gaussian filter to the result. The alpha curve (or just alpha,  $\alpha$ ) is important because it allows for the comparison of the data to a theoretical calculation of the underlying nuclear activity without a detailed knowledge of the absolute calibration of the detection system or the absorbing and scattering effects of the intervening material between the gamma-ray source and the detectors.

After the reaction-history data analysis was completed for an event, a shot report was written to summarize the results of the analysis by recording various  $\alpha$  values and showing graphs of the composite flux and  $\alpha$  curves. Uncertainty analysis consisted of estimating (by eye) the spread of the composite  $\alpha$  curve due to the combination of filtered  $\alpha$  curves from each detector. Toward the end of NTS nuclear testing, rather than comparing calculations to discrete values of the  $\alpha$  curve, more detailed comparisons were being made to try to match calculations to electronic versions of the entire  $\alpha$  curve. When testing ended, the record of the reaction-history measurement for a given event consisted of the event film, which recorded the Rossi traces during the event; logbooks containing experimental setup and calibration information; and a shot report. If the event occurred close to the end of testing, there were also electronic files that contained the flux and  $\alpha$  curves.

Today, there is increased interest in comparing calculations with the most relevant data the nuclear weapons community has: the NTS reaction-history archive. The P-22 Analysis and Archiving Team has two important goals that support several projects, including NTS data archiving, nuclear and nonnuclear data validation, and weapon system certification. The first goal is to train new personnel to understand the experimental aspects of the reaction-history measurement and the analysis of the resulting data and to become familiar with the reaction-history data archive. These new personnel will reanalyze the reaction-history data and interact with the designers, modelers, and computer scientists in the future to help interpret the NTS reaction-history data. The second goal is to preserve the collection of reaction-history data and produce reanalysis and uncertainty estimation in a format that can be used for comparison with calculations.

The P-22 team is currently made up of full-time team members and retirees (who have had direct experience designing and fielding reaction-history measurements at the NTS and analyzing the resulting data) and is also

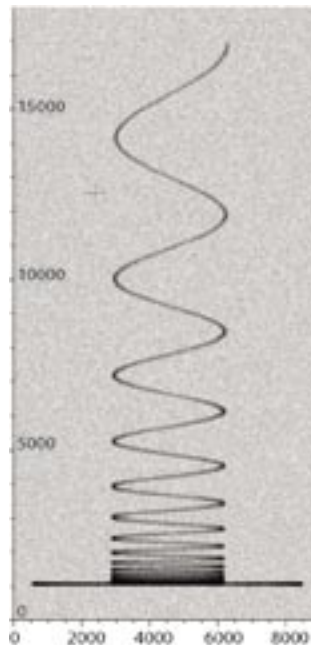


*Figure 10. Simulated film of a Rossi trace.*

supported by Bechtel Nevada. The team is working together to improve the analysis process, to use the new analysis techniques to reanalyze reaction-history data, to develop uncertainty-estimation techniques, and to act as a resource to the weapons community to answer questions about reaction-history measurement and data analysis.

The team is tasked with scanning event films and logbooks to produce an electronic archive of all the reaction-history raw data and with developing and/or improving software that provides computer-aided center-of-trace measurements of event-film images along with an estimation of the uncertainty of the measurement. The team is also tasked with developing techniques and software to provide an estimation of the uncertainty in  $\alpha$  due to film digitization and trace location, flux and alpha calculation, and curve composition and then with applying the new analysis techniques to a prioritized event list.

## Instrumentation Project Descriptions

### Reaction-History Test Readiness

*B.J. Warthen (P-22), representing the Reaction-History Test Readiness Effort*

Since the end of underground nuclear testing at NTS in 1993, the national laboratories involved in performing underground nuclear tests (UGTs) (these include LANL, LLNL, and SNL, and Bechtel Nevada) have been maintaining a 24- to 36-month test-readiness posture. This means that if we are requested to do a UGT, the national laboratories are capable of preparing the necessary experimental diagnostics and logistics for the test within 36 months. This posture is maintained by involving technical personnel in ongoing nonnuclear experiments that produce data and results of interest to the nuclear-weapons community.

When nuclear testing ceased, it was assumed that if a UGT were to be requested in the future, there would be enough experienced personnel remaining (either currently employed at the national laboratories or recently retired and willing to return) and enough existing equipment available that 36 months would provide enough time to get ready. Recently, NNSA has requested that the national laboratories transition to an 18-month test-readiness posture. This change, combined with the realization that the above assumption might not still be valid a full decade after the end of testing, has resulted in a test-readiness program being funded at the national laboratories.

P-22 will work with LLNL, Bechtel Nevada, and SNL to reconstitute the capability to perform a reaction-history measurement on a UGT. P-22's involvement in the test-readiness effort includes the following activities:

- participate in the LANL annual event-design exercise;
- design the reaction-history line of sight and work with DX-5 to incorporate the line of sight into the rack design;
- work with X-5 to calculate detector sensitivities;
- work with Bechtel Nevada to determine the status of existing reaction-history-detection, signal-transmission, and recording systems;
- work with P-21, LLNL, and Bechtel Nevada to identify and test data-recording equipment to replace Rossi oscilloscopes; and
- work with P-21, LLNL, and Bechtel Nevada to develop high-bandwidth-detection, signal-transmission, and recording systems for reaction-history measurements.

### Support of Experiments at the Alternating Gradient Synchrotron

*D.A. Clark, O.F. Garcia, B.J. Hollander (P-22)*

P-22 supports pRad experiments at the BNL AGS. Experiment 963 (E963) was carried out in June 2003. P-22 provided support in the months ahead of the scheduled experiment time to design and install fiber-optic and coaxial cable plants for data-acquisition and control systems. P-22 staff played a major role in design, implementation, and operation of the nuclear-scattering portion of E963, as well as general operations and data acquisition for the entire experiment. After the experiment was completed, P-22 contributed several weeks of effort to reconfigure cable systems in preparation for the next series of experiments at AGS.

### Generation of Energetic Ion Beams Using an Ultra-Short-Pulse, High-Intensity Laser

*J.C. Fernández, J.A. Cobble, B.M. Hegelich, R.P. Johnson, S.A. Letzring, T. Shimada (P-24), J.F. Benage, F.J. Wysocki (P-22), J. Kindel, M.J. Schmitt, D. Winske (X-1), V.A. Thomas (X-4), L.A. Collins (T-4), D.O. Gericke (T-15), J. Kress (T-12), T.E. Cowan, H. Ruhl, Y. Sentoku (University of Nevada, Reno)*

Our work is based on recent progress worldwide in applying short-pulse (subpicosecond) intense ( $\sim 10^{19}$  W/cm<sup>2</sup>) lasers to produce high-current, charge-neutralized ion beams with high conversion efficiency ( $\sim 5\%$  of the laser energy) over a range of light ion species (most commonly protons) with energies in the MeV/nucleon range. Our ultimate goal is to advance our understanding in two areas at the frontiers of plasma physics: (1) relativistic laser-matter interactions, applied towards producing, optimizing, and controlling intense, laser-driven, MeV/nucleon ion beams (including heavy ions); and (2) interactions of beams and dense plasmas in regimes of interest for weapons physics (especially boost in primaries) and for fast-ignition fusion.

We rely on the capability at the LANL Trident laser of collocated long pulses (for laser-plasma formation) and high-intensity short pulses (for relativistic laser-matter interactions). Presently, Trident has the most energetic short-pulse laser in the U.S. The study of the relativistic laser-matter interactions responsible for directed-ion acceleration represents an emerging field of great scientific vitality. Our plasma-physics understanding is presently insufficient to explain fully the underlying processes in such interactions. The process of controlling and optimizing the laser-driven ion acceleration (as part of our upcoming research funded by the LDRD program), will build on recent successes by our team of LANL and external collaborators. Our results can be summarized by three main points.

- (1) In the regime of interest to us, energetic ions are created and accelerated mostly by a transient MV/ $\mu$ m electrical sheath at the rear surface of the target—not at the front surface that is irradiated by the laser.
- (2) The ion beam has a finite divergence, presumably controlled by the physical and geometric characteristic of the sheath, which could be controlled by proper tailoring of the laser-intensity profile or the target geometry.
- (3) These ion beams have a very low transverse temperature. Indeed, a Trident-produced proton beam holds the record for low transverse beam emittance,  $0.0025 \pi$  mm-mrad for 8-MeV protons.

Figure 11 illustrates how this measurement was done, along with a record of the proton beam on a radiochromic film. These results are consistent with the so-called Target-Normal Surface Acceleration model for laser-driven ion acceleration. With untreated metallic targets, most of accelerated ions are protons coming from adsorbed surface contaminants such as water. *In situ* heating of metallic targets to  $> 1,000^\circ\text{C}$  in the vacuum chamber (using electrical currents just before the laser shot) successfully eliminates the hydrogen contaminants and thus results in efficient acceleration of heavier ions. However, joule heating is incapable of removing metallic oxides at the surface of the target, so most of the energy goes into accelerating  $\text{O}^{6+}$  rather than ions from the metallic substrate. Other techniques aimed at removing all surface contaminants are being tested.

The interaction of heavy ions having about MeV/nucleon energies with a background low-Z plasma is relevant in the context of weapons-primary operation. Important fundamental physics aspects in such interactions are neither completely elucidated nor experimentally validated. Many physics uncertainties in primaries are shared with other important areas of current scientific research, such as the properties of planetary interiors (e.g., Jupiter), the grand challenge of achieving fusion ignition in the laboratory, and the properties of dense plasmas. Given the general nature and relevance of the underlying physics, generic experimental configurations can be abstracted to study the issues important in all of these areas. Rather than reproducing the specific conditions in a primary or in a fast-ignition capsule, our aim is to devise a generic experimental configuration to make measurements over a wide range of parameters that are useful for validating emerging theoretical models.

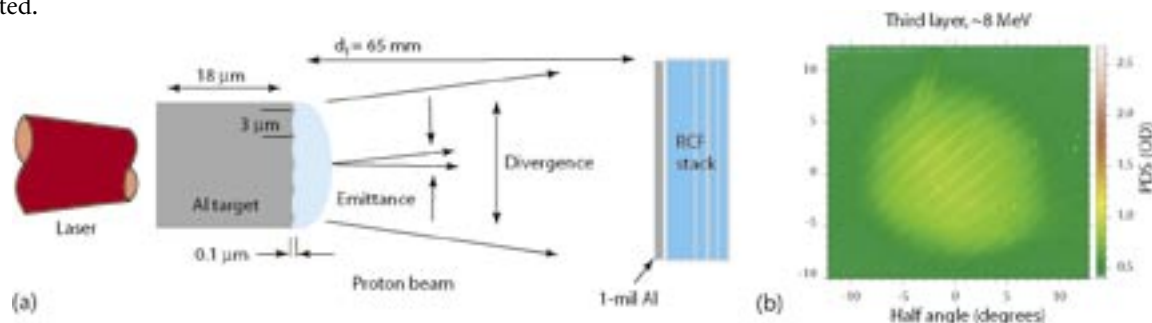


Figure 11. (a) Schematic of the experiment on Trident and (b) record of the proton beam on a radiochromic film.